POLITECNICO DI TORINO
Repository ISTITUZIONALE

Electrical resistivity tomography for the characterization of river embankments: 2D vs 3D inversion

Original
Electrical resistivity tomography for the characterization of river embankments: 2D vs 3D inversion / Pace, F., Arato, A., Vergnano, A., Comina, C., Naldi, M., Godio, A., Socco, L.V.. - In: GEOPHYSICAL JOURNAL INTERNATIONAL. - ISSN 0956-540X. - ELETTRONICO. - 2026:247(2026), pp. 1-23. [10.1093/gji/ggag402]

Availability:
This version is available at: 11583/3017831 since: 2026-11-12T10:15:12Z

Publisher:
Oxford University Press

Published
DOI:10.1093/gji/ggag402

Terms of use:

This article is made available under terms and conditions as specified in the corresponding bibliographic description in the repository

Publisher copyright

(Article begins on next page)

22 November 2026

Geophysical Journal International

Geophys. J. Int. (2026) **247,** 1–23
Advance Access publication 2026 September 30
Research Paper

https://doi.org/10.1093/gji/ggag402

Electrical resistivity tomography for the characterization of river embankments: two-dimensional versus three-dimensional inversion

F. Pace [1], A. Arato,[2] A. Vergnano,[3] C. Comina,[3] M. Naldi,[2] A. Godio[1] and L.V. Socco[1,4]

[1]*Department of Environment, Land and Infrastructure Engineering (DIATI), Politecnico di Torino, Corso Duca degli Abruzzi 24, 10129 Torino, Italy. E-mail: francesca.pace@polito.it*
[2]*Techgea S.r.l., Via Modigliani 26/a, 10137 Torino, Italy*
[3]*Department of Earth Sciences (DST), Università degli Studi di Torino, via Valperga Caluso 35, 10125 Torino, Italy*
[4]*Faculty of Civil Engineering and Geosciences, Delft University of Technology, 2628CN Delft, the Netherlands*

Accepted 2026 September 28. Received 2026 September 7; in original form 2026 January 30

SUMMARY

River embankments are increasingly afflicted by intense and frequent flood events owing to climate change. The characterization and monitoring of river embankments are hence becoming crucial for climate change adaptation. Electrical resistivity tomography (ERT) is one of the most common geophysical techniques for the characterization of river embankments to identify local anomalies and potentially prevent damages during floods. ERT surveys are usually executed over the embankment crest and interpreted along a longitudinal section. However, 2-D interpretation of ERT data can be strongly affected by the embankment morphology along the investigated portion (i.e. the shape of the longitudinal section and the presence of curves). To overcome this issue, we propose 3-D inversion of ERT data acquired over embankments, and compare 2-D and 3-D inversions of both synthetic and field ERT data in order to understand the differences in results between the two approaches. We created a 3-D synthetic model with several types of embedded anomalies to realistically represent the embankment geometry. We considered both a straight and a curved longitudinal profile of the embankment. Synthetic data were then generated with two tailored electrode-configuration arrays (i.e. dipole−dipole and Wenner−Schlumberger). 2-D field data were acquired close to Turin (NW Italy) over an embankment that has often been damaged by floods. The results from 2-D and 3-D inversions were analysed and compared. The main outcomes show that, with synthetic and field ERT data from the crest of the embankment, the subsurface was better characterized by means of 3-D inversion, especially in presence of 3-D eccentric buried features or complex/curved model domains. From the examples of synthetic data, the presence of the embankment slopes and curvatures negatively affected 2-D inversion results, which presented more artefacts and higher misfit values than the 3-D inversion results. From the field case study, the 3-D resistivity volume presented good sensitivity in the transversal direction, thus allowing useful inspection of feature discontinuities or resistivity contrasts. Moreover, for the synthetic data the 3-D results were more coherent than the 2-D results with the true resistivity and position of the anomalies. For the field data, the 3-D results were more coherent than the 2-D results with known information from geological and geotechnical data. The more physically consistent 3-D solutions may be further exploited for quantitative analysis on the petrophysical properties of the embankment material. In conclusion, 3-D ERT inversion is recommended in presence of irregular domains (slopes, curves, strong discontinuities) even with 2-D data.

Key words: Electrical properties; Electrical resistivity tomography (ERT); Numerical modelling; Tomography; Hydrogeophysics.

1 INTRODUCTION

The geophysical characterization of river embankments is nowadays of growing interest because of an increase of frequency and magnitude of floods and extreme events. The management of embankments is becoming crucial among the actions taken for the prevention of floods and, in general, the actions focusing on adaptation to climate change. An adequate monitoring or characterization of river embankments and, specifically, an updated estimation of their geophysical, geotechnical and/or hydraulic properties can lead and improve their maintenance to prevent damages or failures (M.S. Kovačević *et al.* 2018; D. Ghosh *et al.* 2024).

© The Author(s) 2026. Published by Oxford University Press on behalf of The Royal Astronomical Society. This is an Open Access article distributed under the terms of the Creative Commons Attribution License (https://creativecommons.org/licenses/by/4.0/), which permits unrestricted reuse, distribution, and reproduction in any medium, provided the original work is properly cited.

Downloaded from academic.oup.com/gji/article/247/3/ggag402/8853762 by guest on 16 November 2026

Electrical resistivity tomography (ERT) is one of the most common geophysical techniques employed for the characterization of river embankments thanks to its high sensitivity to water saturation, infiltration paths and other subsurface discontinuities owed to the electrical resistivity variations (M.H. Loke *et al.* 2013; M.T. Perri *et al.* 2014; G. Tresoldi *et al.* 2019; J. Ball *et al.* 2023; A. White *et al.* 2024). Typical features that can be found inside an embankment are the burrows of fossorial animals, fissures, pipelines, metallic nets, bulkheads and concrete units, that can generate resistivity anomalies detectable by ERT data. Other geophysical methods typically applied to river embankment characterization are Ground Penetrating Radar (S. Negri *et al.* 2008; M. Di Prinzio *et al.* 2010; M.T. Perri *et al.* 2014; R. Antoine *et al.* 2015; A. White *et al.* 2023) and surface waves and/or seismic refraction (e.g. L. Karl *et al.* 2011; C. Comina *et al.* 2020), that sometimes are simultaneously acquired with resistivity data (C. Chen *et al.* 2006; L. Busato *et al.* 2016; S. Rahimi *et al.* 2018; A. Arato *et al.* 2022; F. Vagnon, C. Comina & A. Arato 2022, F. Vagnon *et al.* 2022; C. Comina *et al.* 2025, 2026; A. Vergnano *et al.* 2025a).

ERT data are usually acquired following the longitudinal direction of the embankment over its crest and then processed according to a 2-D inversion approach (T. Dahlin 1996; M. Gharibi & L.R. Bentley 2005; L. Busato *et al.* 2016; G. Bièvre *et al.* 2018; A. Arato *et al.* 2022). However, the typical embankment geometry, composed of a crest on the top and two lateral slopes laying over a large basis, is 3-D and may not be suitable for 2-D interpretation (M.H. Loke 2004), particularly in areas with complex geology and punctual anomalies (M.H. Loke *et al.* 2013; R. Martorana & P. Capizzi 2023). Moreover, the sensitivity kernel of the resistivity measurements over embankments corresponds to a volume that is affected by objects and features that are not 2-D. This creates artefacts in the 2-D resistivity model that is retrieved by 2-D inversion (D. Arosio *et al.* 2018; A. Hojat *et al.* 2020). Previous works have addressed this issue by introducing some correction factors to account for the 3-D effects for both the embankment geometry (D. Arosio *et al.* 2018; G. Bièvre *et al.* 2018; G. Tresoldi *et al.* 2019; A. Hojat *et al.* 2020; A. Hojat 2024; A. White *et al.* 2024) and other 3-D configurations (T. Günther *et al.* 2006; Y.-C. Hung *et al.* 2019). Other works have compared 2-D and 3-D approaches to study remediation sites (L.R. Bentley & M. Gharibi 2004; M. Gharibi & L.R. Bentley 2005; R.E. Nimmer *et al.* 2008) or archaeological sites (N.G. Papadopoulos *et al.* 2007; A.K. Lysdahl *et al.* 2017; A. Vergnano *et al.* 2025b). Currently, 3-D ERT surveys are not routinely carried out, but they are becoming more feasible than in the past in terms of field instrumentation, acquisition time, computation cost and software availability (T. Dahlin & M.H. Loke 1997; C. Rücker *et al.* 2006; S. Negri *et al.* 2008; J.E. Chambers *et al.* 2012; J. Boyd *et al.* 2019; A. Vergnano *et al.* 2025b). However, little work has focused on 3-D direct and inverse modelling of ERT data acquired over the crest of the embankments.

For embankment characterization and monitoring, the 3-D approach would be particularly relevant because the embankment geometry represents a constraint to the electric field propagation, and the embankment structure may contain features (e.g. reinforcements, protections) that are located laterally on the slopes. The advanced 3-D inversion and meshing tools that are nowadays available make feasible 3-D inversion of 2-D data, so it may become convenient to carry out 3-D inversion to reduce the inversion artefacts, while keeping the acquisition 2-D and cost effective. The scientific question that arises is: 'Given that ERT data from embankments present 3-D effects due to 3-D geometry and 3-D buried features, could it be advantageous to perform 3-D inversion of a 2-D ERT line instead of only 2-D inversion?' or, in other words: 'Is 2-D inversion of an ERT line adequate in presence of 3-D buried bodies or of 3-D domain geometries like an embankment?'.

The objectives of this work are to demonstrate both the effects of three-dimensionality on ERT data from a 2-D acquisition and the potential advantages of performing 3-D inversion instead of 2-D inversion for a proper subsurface characterization of the embankment, even in presence of a 2-D ERT line. The novelty of this study relies on the full 3-D approach for the embankment, meaning that the forward and inverse modelling of ERT data were performed in 3-D by using a customized 3-D model of a realistic embankment and not a general blocky model.

Both synthetic and field data were considered, acquired in 2-D following the longitudinal direction of the embankment. The synthetic data were generated from a 3-D model including several anomalies with different resistivity and size, in order to simulate some common features hosted in an embankment. A 300m-long synthetic model was created with both straight and curved longitudinal profiles representing diverse field conditions. We created the straight and curved synthetic models to demonstrate that ERT data from a 2-D profile can be influenced by both 3-D buried geometries (that could be below the line, eccentric or far) and by the three-dimensionality of the model domain (e.g. the embankment slopes or longitudinal curve). The field data came from an embankment in Verolengo, a town nearby Turin (Piedmont region, NW Italy), that has been frequently afflicted by floods. The ERT profile was acquired on the crest of the embankment and was composed of 288 electrodes (1 m of spacing). Geotechnical data and geological information were available to support the geophysical results. The 3-D models were specifically created by using Gmsh (C. Geuzaine & J.-F. Remacle 2009), while 2-D and 3-D modelling were carried out in ResIPy (G. Blanchy *et al.* 2020). The added value of this work is the publication in the Supplementary Material of the ERT electrode sequences, the python notebook used to create the 3-D models and meshes, the files of the meshes adopted, the synthetic data and the ResIPy results from 2-D and 3-D inversion of synthetic data. They are publicly available in Zenodo, at https://doi.org/10.5281/zenodo.17965478.

The ensuing sections present at first the methodology and software adopted. Then, the synthetic and field case studies are described. Finally, the results are widely shown and discussed. In addition, a detailed Appendix presents further inspections on the data and results as well as on the creation of the customized models and meshes. Complementary work about the data reported in this paper has been presented in F. Pace *et al.* (2025) and A. Vergnano *et al.* (2025a).

Downloaded from academic.oup.com/gji/article/247/3/ggag402/8853762 by guest on 16 November 2026

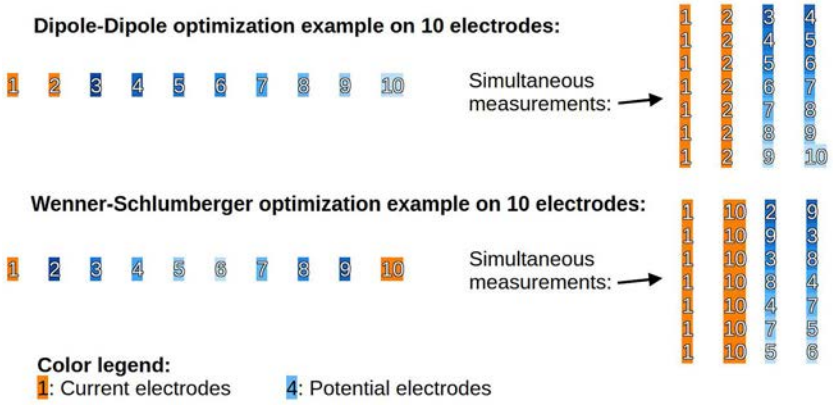


Figure 1. The optimization of the sequences for DD (top) and WS (bottom) configurations for the ERT survey over the embankment. Example of a current dipole (electrodes nos. 1 and 2 for DD, 1 and 10 for WS) and relative potential measurements (electrodes nos. 3 to 10 for DD, 2 to 9 for WS) for a single measurement with 10 electrodes.

2 METHODOLOGY

The ERT method is an active geophysical technique that applies a direct current to the transmitter dipole and record the induced voltage at the receiver dipole (Tikhonov & Arsenin 1977; Koefoed O. 1979; A. Binley 2015; Binley & Slater 2020). The quadrupoles can be distributed on the ground following different configurations that are sensitive to different patterns of the subsurface resistivity (M.H. Loke 2004).

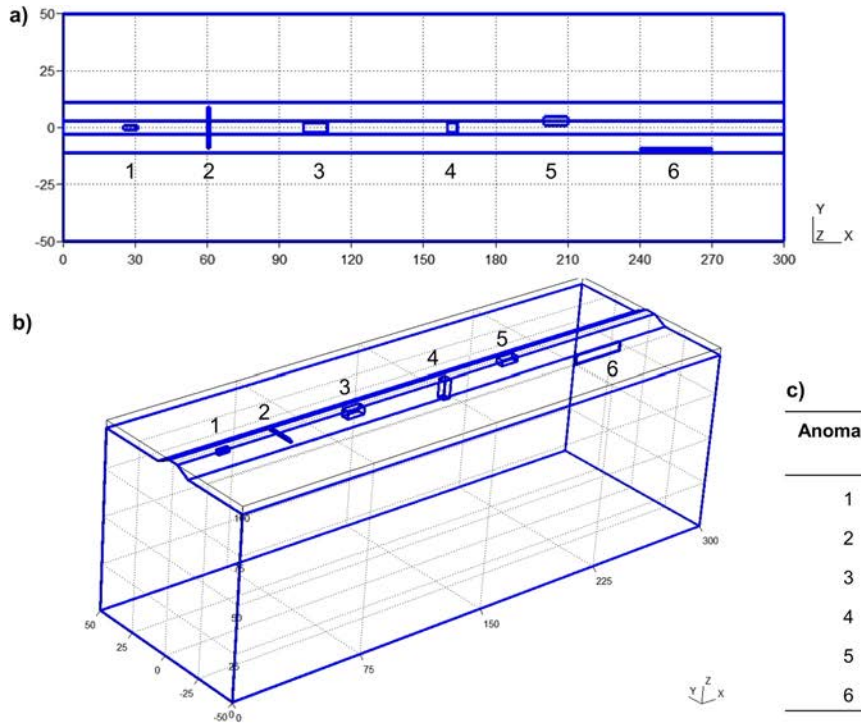
In this study, for both synthetic and field data, the first ERT data acquisition had 1m-spaced 72 electrodes, which were combined with nine roll-along acquisitions, each composed of 24 electrodes. In total, the ERT line had 288 electrodes and was 287 m long. The electrode spacing of 1 m is commonly adopted for the characterization of long portions of embankments because it is cost-effective and at the same time it ensures an adequate depth of investigation from the embankment body up to the foundation basement, that sometimes can be a relevant target of investigation (L. Busato *et al.* 2016; G. Tresoldi *et al.* 2019; A. White *et al.* 2024). Moreover, the spacing of 1 m was identified as an ideal compromise between data resolution and acquisition efficiency after some tests for the seismo-electric streamer of the GEOCHARME project (GEOphysical CHARacterization and Monitoring of Earthen dams and levees), devoted to river embankments (C. Comina *et al.* 2025, 2026). For our case study, the electrode spacing of 1 m was motivated by the desired depth of investigation of around 8 m to characterize anomalies inside the embankment body and in the upper part of the foundation basement. Electrode spacings shorter than 1 m were not considered since they would have decreased the investigation depth and lengthened the fieldwork activity.

Two quadrupole configurations were employed: dipole–dipole (DD) and Wenner– Schlumberger (WS). DD is sensitive to lateral resistivity contrasts, while WS is sensitive to the vertical layering of the subsurface (A. Binley & A. Kemna 2005; R. Martorana *et al.* 2017). The DD and WS sequences were optimized on purpose to reduce the investigation time and maximize the number of data and depth coverage. While DD optimization is a relatively standard approach, WS optimization is less commonly adopted. We optimized the WS sequence by setting, for example, the current electrodes to 1–10, and the potential electrodes relative to those current electrodes to 2–9, 9–3, 3–8, 8–4, 4–7, 7–5 and 5–6. Fig. 1 illustrates an example of the scheme of the optimized DD and WS configurations. The current dipole is shown in orange, while the potential dipoles associated to it are in shades of blue. The roll-along sequences were also designed in order to prevent repeated measurements after moving one cable ahead in the measurement line (1 cable corresponds to 24 channels). In total, attaching the main sequence and all the nine roll-along sequences, we obtained around 29k quadrupoles for the DD sequence, and around 27k quadrupoles for the WS sequence. Both the creation of ERT synthetic data and the fieldwork at the Verolengo test site made use of these sequences. They are published in the Supplementary Material, including the custom R scripts used to generate them.

The ERT modelling (forward and inverse) was carried out by using the software ResIPy (v. 3.6.3), an open-source package that performs 2-D and 3-D modelling of direct current and induced polarization data (J. Boyd *et al.* 2019; G. Blanchy *et al.* 2020; Y.G. Doyoro *et al.* 2022; https://gitlab.com/hkex/resipy). ResIPy is based on the freeware packages R2, cR2 and R3t (A. Binley & A. Kemna 2005; A. Binley 2023, 2024), which perform a weighted least-squares inversion of the data with Occam's regularization (A. Binley & A. Kemna 2005; A. Binley 2015). The settings for 2-D and 3-D inversions were the regularized inversion with linear filtering and normal regularization and can be inspected in the Supplementary Material (see files 'R2.in' and 'R3t.in' in the inversion folders). For further details about inversion in ResIPy see the R2 manual (A. Binley 2023) and the R3t manual (A. Binley 2024). The 3-D inverse modelling was executed in a workstation with a CPU model Intel Core i7-6950×3 GHz with 128 GB of RAM.

ResIPy includes a model generator based on the electrode positions and a mesh generator based on the software Gmsh (C. Geuzaine & J.-F. Remacle 2009; http://gmsh.info). Gmsh is an open-source tool suitable for the creation of complex meshes. It can be downloaded and executed from a GUI (graphical user interface) or controlled with C++, C, Python, Julia and Fortran programming interfaces. For

Downloaded from academic.oup.com/gji/article/247/3/ggag402/8853762 by guest on 16 November 2026



c)

Anomaly n.	Resistivity (Ωm)	Length Δx, Δy, Δz (m)	Depth of top b.g.l. (m)
1	10	6, 2, 2	1
2	1000	1, 20, 1	1
3	10	10, 4, 4	1
4	10	4, 4, 10	1
5	10	10, 4, 3	2
6	1	30, 0.7, 5	5

Figure 2. The straight 3-D synthetic model with the six embedded anomalies created in Gmsh: (a) top view; (b) 3-D view to show the slopes and crest of the embankment; (c) details of the six bodies of anomalies: ID, resistivity value, length of the three dimensions, depth of the top surface b.g.l.

2-D inversion, we adopted the model and mesh generator of ResIPy, that internally calls Gmsh automatically. For 3-D inversion, since the default 3-D model generation in ResIPy would not have included the embankment slopes, we chose to externally control the model creation in Gmsh to accurately reproduce the 3-D embankment geometry. We worked in Gmsh from Python JupyterLab. The final 3-D model included a straight or curved crest hosting the electrode line, the lateral slopes and the embankment basement. We did not evaluate the water level on the river side of the embankment because our research focuses on the characterization of embankments for monitoring or prevention and not for the management during extreme events. Geotechnical and hydrogeological implications such as infiltration pathways or structural failures were hence not considered since they are beyond the scope of this work. The 3-D mesh was tuned in Gmsh to ensure a fine discretization close to the electrodes and an adequate number of total nodes to make acceptable the modelling runtime in ResIPy. The creation of the 3-D models and meshes is accurately explained in Appendices B and C (Supplementary Material). The Supplementary Material includes the Python notebook (a '.ipynb' file) that reproduces all the models and meshes presented in this work.

3 SYNTHETIC MODELS

The 3-D synthetic model was conceived to simulate an embankment hosting different anomalies. The body of the embankment has a 300m-long and 6m-wide crest and a vertical/horizontal slope ratio of 1:2. The height of the embankment is 4 m, because it is the average value of the embankment height of the field case study. The base of the embankment is 22 m large and is surrounded by a wide domain in the three dimensions to ensure proper boundary conditions for ERT modelling. The whole 3-D model represents the embankment in the longitudinal direction (*X*-direction) and has both width (*Y*-direction) and depth (*Z*-direction) of 100 m (Fig. 2). The minimum distance between the centre of the 3-D anomalies and the model boundaries is 28–30 m in *X*-direction and 40 m in *Y*-direction. The distance between the centre of the 3-D anomalies and the bottom of the model (*Z*-direction) is in the range 94–98.5 m. These model settings avoided any artefacts owed to boundary conditions in the generation of the synthetic data. Given these features, two different synthetic models were created, a straight one and a curved one, the latter to simulate realistic conditions potentially encountered in the field.

The straight synthetic model is shown in Figs 2(a) (top view) and (b) (3-D view). The curved synthetic model is shown in Figs 3(a) (top view) and (b) (3-D view). The synthetic models were populated with six anomalies having different sizes, shapes, eccentricity to the electrode line and resistivity values (ρ), as listed in Fig. 2(c). Apart from large-scale differences in the embankment material, these anomalies represent the main features that can be encountered inside a real embankment: structural discontinuities, animal burrows, buried walls or pipelines. The embankment height of 4 m allowed these anomalies to be located in different positions with respect to the embankment body: Anomalies nos. 1 and 2 are inside the embankment, nos. 3 and 5 are at the bottom of it and nos. 4 and 6 are below it. Anomaly no.1 is a shallow box with $\rho = 10$ Ωm, possibly representing an infiltration zone or clayish material. Anomaly

Downloaded from academic.oup.com/gji/article/247/3/ggag402/8853762 by guest on 16 November 2026

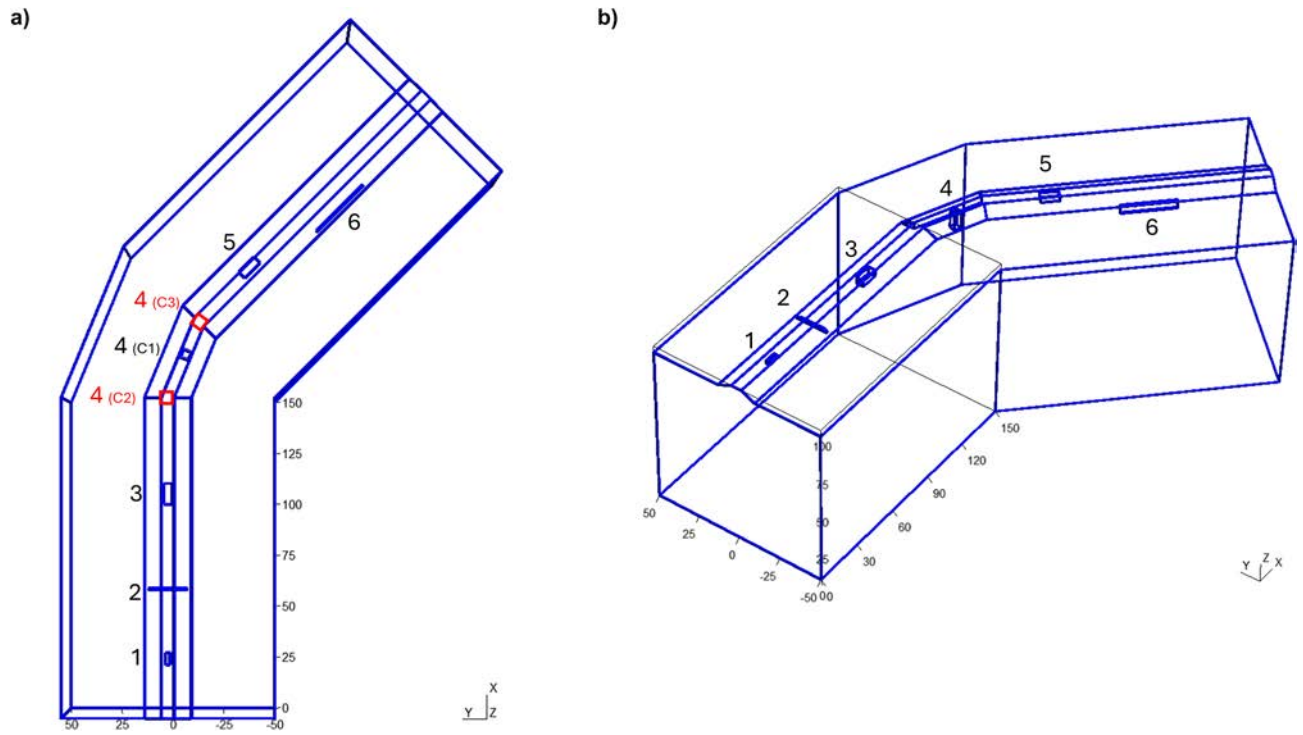


Figure 3. The curved 3-D synthetic model with the six embedded anomalies created in Gmsh: (a) top view of the curved model with anomaly no. 4 located in three different positions: in the middle of the wedge for model C1, at the end of the straight branch for model C2 and at the beginning of the oblique branch for model C3; (b) 3-D view of model C1.

no. 2 is a long thin box with $\rho = 1000$ Ωm that transversally crosses the embankment from slope to slope simulating a cavity or an animal burrow. Anomaly no. 3 is a large horizontal box with $\rho = 10$ Ωm, possibly representing the remains of an abandoned metallic pipeline that has been mixed or filled with concrete (or other resistive material) to avoid structural failure, like the drainage pipe found in A. Arato *et al.* (2022). Anomaly no. 4 is a long vertical box that ends below the embankment body and has $\rho = 10$ Ωm, possibly representing a metallic bulkhead or a strong lateral discontinuity of the embankment material. Anomaly no. 5 is an eccentric box below the edge between the crest and the slope of the embankment and has $\rho = 10$ Ωm, possibly representing a metallic net used to hamper the tunnels of fossorial animals. Anomaly no. 6 is a thin, eccentric (the transversal distance from the embankment axis is 10 m) and deep box below the slope and has $\rho = 1$ Ωm to simulate a thin diaphragm of reinforced concrete containing a high density of steel rebars or an electro-welded steel mesh (as found in A. Arato *et al.* 2022). Further details about the length and depth of the six anomalies are listed in Fig. 2(c). The background resistivity of the model was 100 Ωm, as a trade-off value among the anomaly resistivities. The chosen background resistivity is intended to represent typical embankment properties in North–West Italy, usually built with natural materials (sands and gravels) exploited from surrounding caves or directly from river deposits (C. Comina *et al.* 2020a). The reason for the homogeneous background is that setting different resistivities in the starting domain (e.g. top/bottom or left/right) would have heavily biased both forward and inverse modelling. A homogeneous background allowed the local anomalies to be clearly identified, at the expense of potentially neglecting large-scale variations in the material below the embankment.

For the curved synthetic model, a sensitivity analysis was carried out on anomaly no. 4, which was placed at three different locations (see Fig. 3): in the middle of the wedge (model C1), at the end of the straight branch (model C2) and at the beginning of the oblique branch (model C3).

The 3-D synthetic model described above was adopted to generate through 3-D forward modelling a synthetic data set. The data acquisition simulated in the 3-D forward modelling was composed of a single ERT line. Forward modelling was performed in 3-D to consider the realistic 3-D current flow in the embankment. Then, this data set storing 3-D information was inverted in both 2-D and 3-D. This choice links with the field application of our study: In an embankment-like structure, a real measurement will always be a '3-D forward', in which the electrical current can flow in the 3-D space but constrained by the embankment slopes.

The model and mesh for 2-D inversion were not extracted from the 3-D synthetic model but were specifically created in ResIPy. The mesh for 2-D inversion had around 6k nodes. For 3-D forward and inverse modelling, two different 3-D models and meshes were externally created in Gmsh (see Appendix B for further details and the Gmsh commands in Supplementary Material). While the 3-D model for forward modelling included the bodies of the anomalies, the 3-D model for inversion had no bodies inside, in order not to bias the resistivity reconstruction during the inversion process.

To run 3-D forward modelling, the electrode positions and the DD and WS sequences were imported in the ResIPy project. The customized Gmsh 3-D model containing the mesh was imported as a '.msh' file. The anomalies and the surrounding volume were

Downloaded from academic.oup.com/gji/article/247/3/ggag402/8853762 by guest on 16 November 2026

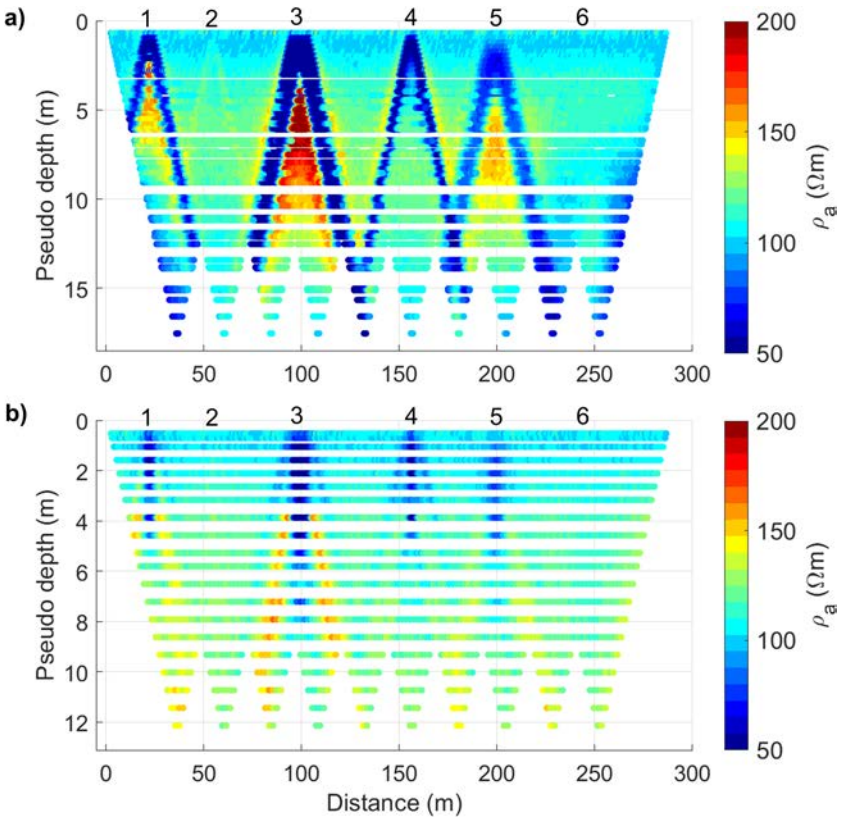


Figure 4. The apparent resistivity pseudo-sections from synthetic data of the straight model S1 after 3-D forward modelling: (a) DD and (b) WS configurations. The location of the six anomalies is reported on the top of each pseudo-section.

numbered as a specific zone of modelling and associated with their resistivity value. Finally, 2 per cent of Gaussian noise was added to the synthetic data. 3-D forward modelling required around 1.2−1.5 GB of total memory and lasted around 5 min. Then, DD and WS synthetic data were used for 2-D and 3-D inversion.

For 2-D inversion, the standard deviation of the measurements was set by means of the error model parameters '*a_wgt*' and '*b_wgt*', which were 0.01 and 0.02, respectively, as suggested in A. Binley (2023). They mean an offset error of 0.01 Ω on the resistance data and a relative error of 2 per cent (further details in A. Binley 2023). The smoothing parameter was 1, as default, to avoid any smoothing anisotropy during inversion, that is, any preferred horizontal/vertical direction of smoothing. The settings for 3-D inversion were the default settings of ResIPy. We checked the advanced setting '*do not crop the output*' in order to retrieve the full 3-D resistivity model (and not a subvolume below the electrodes) at the end of the inversion.

3.1. *The three-dimensional straight model*

The straight 3-D model is 300 m long (*X*-direction), with both width (*Y*-direction) and depth (*Z*-direction) of 100 m to ensure proper boundary conditions (Fig. 2). In fact, even though the electrode spacing of 1 m would have suggested a shallow model, the depth of 100 m was necessary to minimize the effect of deep resistivity artefacts of the 3-D forward model response.

The electrode line was placed in the centre of the embankment crest (represented by the $Y = 0$ axis) and also in two different shifted locations, that is, on the axes $Y = 2$ m and $Y = -2$ m. Thereafter, these configurations are called S1, S2 and S3 models, respectively. These three different positions of the ERT line were conceived as a sensitivity analysis to inspect the effects of the closeness of the electrodes to the buried anomalies and the effects of the edge between the crest and the slope.

The meshes adopted for the tests with the electrode line at $Y = 0$, $Y = 2$, $Y = -2$ were quite the same, except for slight adaptations to impose the electrode positions in correspondence to the mesh nodes, as necessary for a correct 3-D inverse modelling in ResIPy.

The apparent resistivity pseudo-sections generated from the 3-D straight model with the electrodes on the $Y = 0$ axis are depicted in Figs 4(a) and (b) for DD and WS configurations, respectively. The location of the six anomalies on the *x*-axis is also written on the top of Figs 4(a) and (b) to partially relate the apparent-resistivity variation to the synthetic body that generated it. The main difference between the DD and WS pseudo-sections confirms that the DD configuration emphasizes the horizontal resolution and the vertical elongation of the structures. The pseudo-sections from models S2 and S3 are shown in Appendix A (Supplementary Material).

Downloaded from academic.oup.com/gji/article/247/3/ggag402/8853762 by guest on 16 November 2026

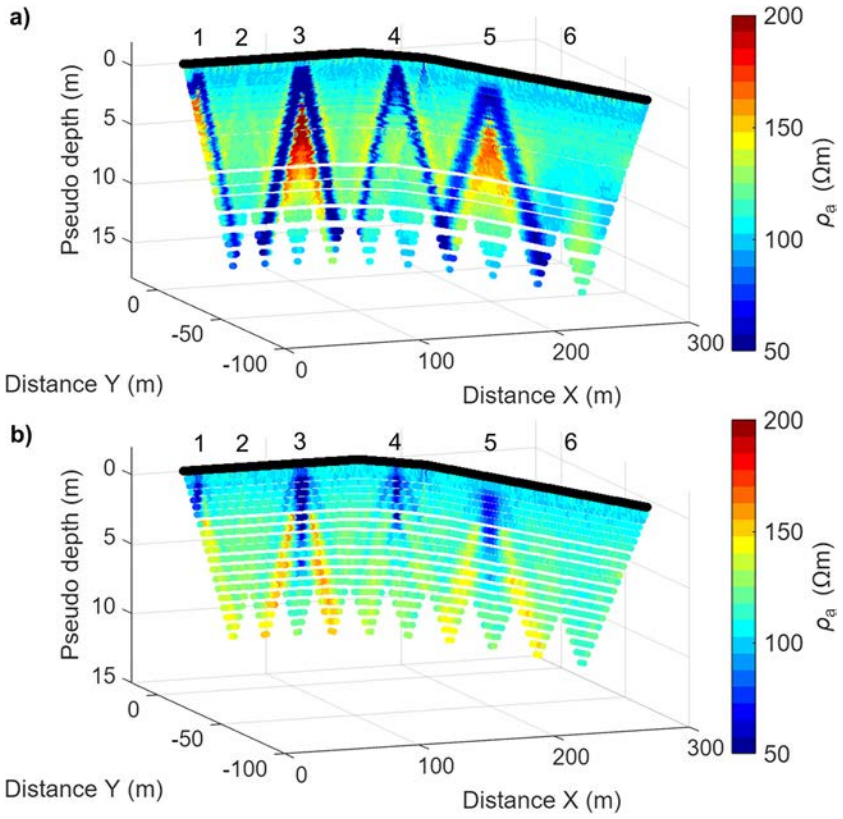


Figure 5. The 3-D visualization of the apparent resistivity pseudo-sections from synthetic data of the curved model C1 after 3-D forward modelling: (a) DD and (b) WS configurations. The black dots represent the electrodes. The location of the six anomalies is reported on the top of each pseudo-section.

3.2. *The three-dimensional curved model*

The curved 3-D model is 100 m wide (*Y*-direction), 100 m deep (*Z*-direction) and 338 m long (longitudinal direction). This geometry simulates a realistic embankment following a smooth bend of a river. The model was built in Gmsh as the union of three volumes (see Fig. 3): a 150 m-long straight branch, a 38 m-long wedge and a 150 m-long oblique branch. This branch has an inclination of 45° with respect to the straight branch. On the top of the basement, the embankment geometry was created. Its crest hosts the 288 m-long ERT line, which starts at $X = 20$ m and follows the curve. The six anomalies inside the model are the same as the straight model (see Fig. 2c), except for their coordinates in the oblique branch. The curved models C1, C2 and C3 were created to inspect the effects of a resistivity contrast in coincidence of a geometric discontinuity.

The pseudo-sections of apparent resistivity data generated from the C1 model are depicted in Figs 5(a) and (b) for DD and WS configurations, respectively. At both sides of the conductor corresponding to anomaly no. 4, there are two slight conductive effects due to the corners of the curved model. The pseudo-sections from models C2 and C3 are shown in Appendix A (Supplementary Material).

4 FIELD DATA

ERT field data were acquired over a river embankment located in Verolengo, a town close to Turin (Piedmont, NW Italy). The embankment, in the left bank of the Po River, is 2.5 km long to reduce the vulnerability of the residential area with respect to floods. It was designed to resist a flood with a calculated return time of 200 yr, as prescribed by the Floods Directive /60/EC of the European Parliament (Floods Directive 2007). The distance between the embankment and the riverbank ranges from 200 to 1000 m. The areas beyond the embankment have been flooded during several extreme events in November 1994, October 2000, November 2016 and April 2025. The embankment crest is large around 6 m and its height varies between 2.5 and 5 m above the ground level throughout the 2.5 km of the embankment length. The slopes have a vertical/horizontal ratio of 1:2.

The ERT data were acquired in July 2024, when the embankment and the floodplain were dry, and the Po River had a low water level. The riverbank was around 500 m far away from the ERT line, so the water level was not measured. The base acquisition was composed of 72 electrodes, then nine roll-along acquisitions (24 electrodes each) were added. In total, the ERT line had 288 electrodes with a reciprocal spacing of 1 m (red line in Fig. 6a). The crest of the embankment has been raised in 2023 to better resist against the frequent and severe floods. Fig. 6(b) is a picture of the last flood in April 2025, taken from the portion of the embankment here analysed. The building site in 2023 was divided into two lots ('LOT 1' and 'LOT 2' in Fig. 6c), characterized by different settings of the materials

Downloaded from academic.oup.com/gji/article/247/3/ggag402/8853762 by guest on 16 November 2026

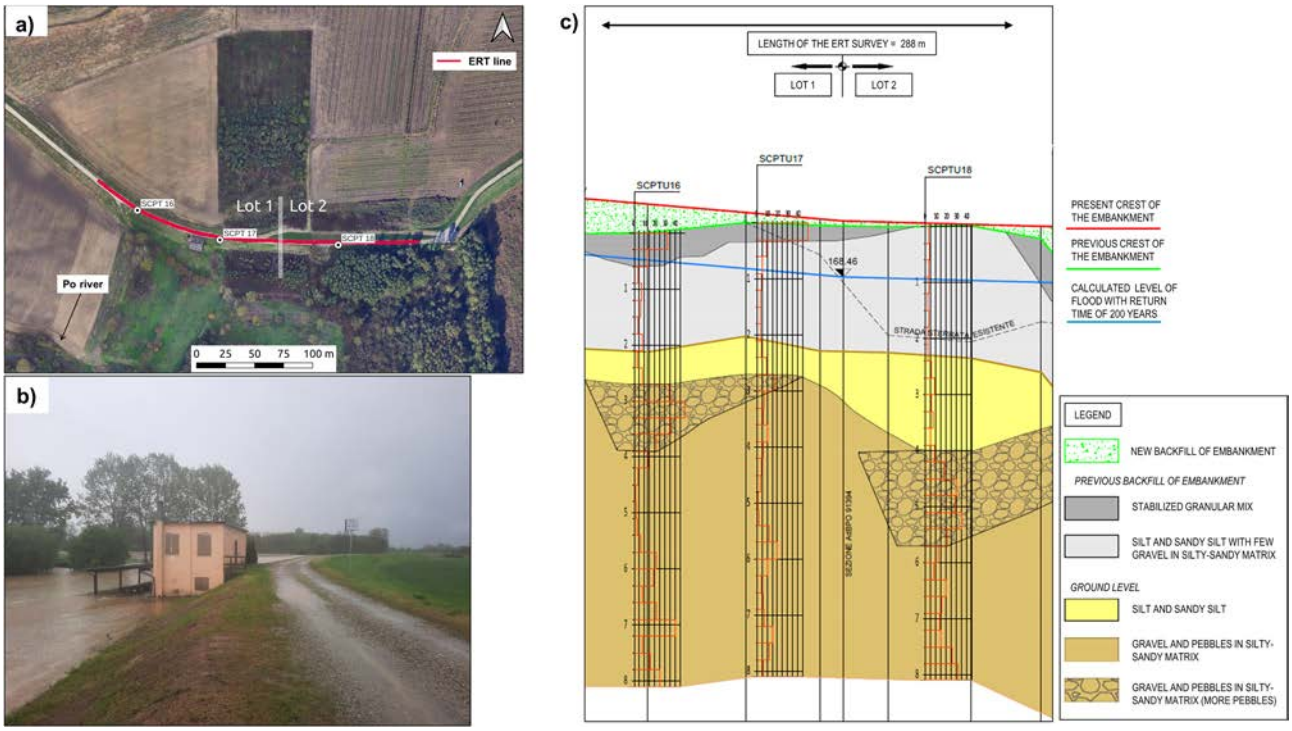


Figure 6. (a) The area of the ERT survey in Verolengo with the position of the ERT line highlighted on the top of the embankment; (b) a picture of the flood that in April 2025 affected the portion of the embankment where the ERT survey was conducted (courtesy of AIPO, Interregional Agency for the Po River); (c) the geological scheme of the embankment distinguishes the ground level (sandy silt and gravels-pebbles) from the embankment (previous and new) backfill. Geological scheme from geotechnical investigations carried out by AIPO. The location and data of the SCPTs are superimposed.

used during the working activities. The length of the ERT survey is highlighted with a black arrow on the top of Fig. 6(c). The division of the two lots lies in the middle of the ERT line, at electrode no. 164. Fig. 6(c) illustrates background information about the embankment, consisting of a geological sketch and three Standard Cone Penetration Tests (SCPTs) from SCPT16 to SCPTU18. In the embankment section, the red line depicts the crest of the embankment at the date of the geophysical survey (2024), while the green line represents the previous crest, before the construction site in 2023. The blue line represents the expected level of the flood with a calculated return time of 200 yr. The actual crest is around 1 m above that expected flood level. The geological units represent the ground level (yellow and brown areas) and the embankment backfill (grey and green areas). The material of the units in grey has been modified during the construction site and mixed with new clayish material to create the new crest. The current lithology of the embankment, as confirmed by local geotechnical investigations, is characterized by a shallow stabilized natural mixture, related to the road on the top, followed by the silty clay material of the embankment backfill up to about 3 m depth. In the foundation soil below the embankment, a silty–sandy formation was observed with localized presence of compacted gravels and pebbles. The water table is expected at around 5−10 m depth b.g.l. The data from the three SCPTs plotted in red in Fig. 6(c) represent the number of blow counts, an indicator of soil stiffness that can be correlated with the electrical resistivity. The SCPT blow counts are generally directly proportional to the resistivity (A. Devi *et al.* 2017; J.T.D. Gonçalves *et al.* 2021), but the linear relationship is not universal and is site-specific (S. Oh & C.-G. Sun 2008; K. Sudha *et al.* 2009). For the three SCPTs, the blow counts increase below the embankment at the level of gravel and pebbles.

The ERT data were collected with the georesistivimeter Syscal Pro (Iris instruments). Standard stainless-steel electrodes were used. The injection time of current was 250 ms, with 3 to 6 stacks according to a maximum standard deviation of 2 per cent. In order to allow for occasional vehicle transit, the electrodes were positioned slightly aside from the centre of the embankment crest, and, specifically, they were relocated towards the northern slope, approximately one metre far from the embankment slope. After checking the electrical coupling, the contact resistance was lowered to maximum 10 kΩ by irrigating the electrodes that presented high values. The raw data were filtered and processed in Prosys-III (Iris Instruments), that allows advanced data processing. The overall quality of the data was very high and only 3 and 8 per cent of the original measurements were discarded as outliers for DD and WS data, respectively. These outliers were anomalous values of apparent resistivity, current and voltage, and were outside the main data cluster. After the outlier removal, the maximum standard deviation of the remaining data was 5 per cent, so no further thresholds were applied to them. The reciprocal measurements of DD data were acquired. Figs 7(a) and (b) show the apparent resistivity of field data for DD and WS configurations, respectively.

The mesh for 2-D inversion was directly generated in ResIPy and had around 5700 nodes. The geographical elevation of the electrodes was included in 2-D inversion.

Downloaded from academic.oup.com/gji/article/247/3/ggag402/8853762 by guest on 16 November 2026

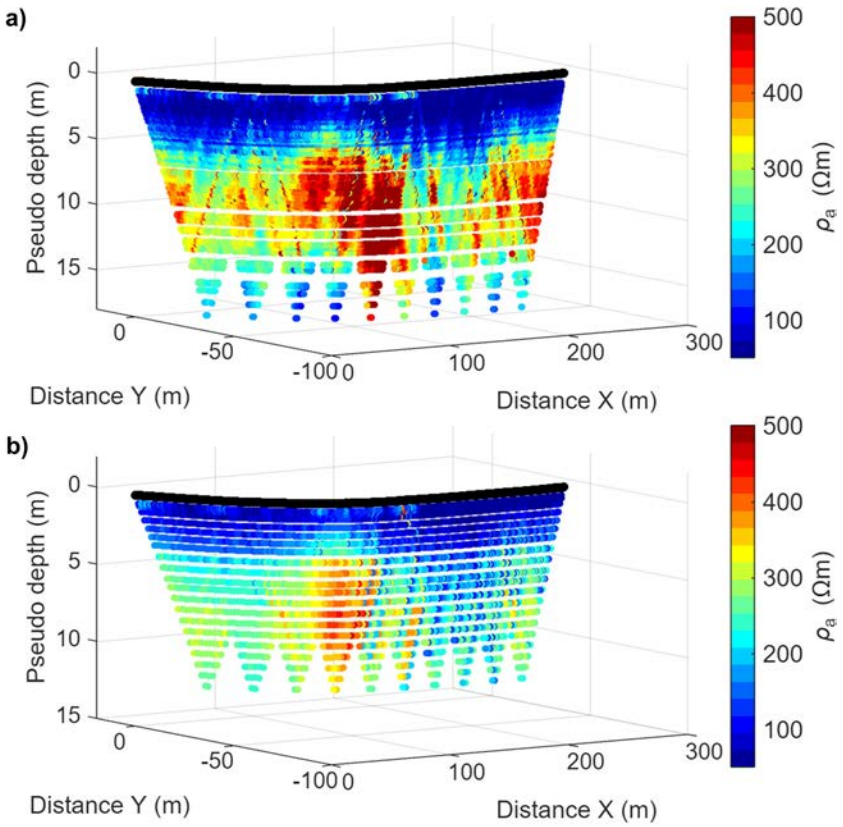


Figure 7. The 3-D visualization of the pseudo-sections of apparent resistivity of the ERT data from Verolengo for (a) DD and (b) WS configurations. The black dots represent the electrodes.

For 3-D inversion, a realistic 3-D model was created in Gmsh to include the slightly curved ERT line and the geometry of the real embankment (see Fig. 8). In the model, the embankment height is 3 m because it is the true height of the embankment portion investigated by the ERT survey. The slopes have a vertical/horizontal ratio of 1:2, as in the synthetic models. The crest is 5.2 m large. The total height of the model is 100 m (Z-axis), the length 350 and 130 m in the X and Y-directions, respectively, as shown in Fig. 8, where the yellow dots represent the electrodes embedded into the mesh. The position of the electrodes is as in the field. The custom-made 3-D mesh had 84k nodes, as shown and described in detail in Appendix C (Supplementary Material).

5 RESULTS FROM SYNTHETIC DATA

Both 2-D and 3-D inversions were initialized with a homogeneous starting model of 100 Ωm, as commonly used (A. Binley 2023). The value of 100 Ωm was a trade-off among the resistivity of the six anomalies. A heterogeneous starting model (e.g. horizontally layered) would have unnecessarily biased the inversion results with the presence of artefacts not justified by the data. Moreover, given that the maximum investigation depth of the data set was around 8–10 m, any prior structures placed below it would have had no sensitivity. Therefore, no other starting models were tested. The inversion results were preliminary analysed in ResIPy, then plotted in Paraview (C.D. Hansen & C.R. Johnson 2005) for a proper visualization. The following figures of the results are overlapped with the edges of the true anomalies to ease the comparison. All the sections were cut at 15 m of depth b.g.l., which is the region of interest. In this Section, the term 'conductive' refers to resistivity values less than 30 Ωm ($\log_{10}\rho = 1-1.5$ Ωm), while the term 'resistive' refers to resistivity values higher than 300 Ωm ($\log_{10}\rho = 2.5-3$ Ωm).

5.1 *Results for S1 model*

A 2-D section of the true 3-D synthetic model with the six anomalies in the XZ plane is represented in Figs 9(a) and 10(a). The projection of anomaly no. 6 is shown with a dashed contour because it is not directly below the electrode line, but eccentric at $Y = -10$ m (see Fig. 2). Figs 9 and 10 represent the results from 2-D and 3-D inversions, respectively. Panels (b) and (c) show the resistivity models for DD and WS configurations, respectively, while panels (d) and (e) show the model misfit for DD and WS configurations, respectively. Figs 9(b) and (c) represent the 2-D models as resulted from 2-D inversion. For the plots in Fig. 10, the vertical slice below the electrode line was extracted from the 3-D model. The model misfit was calculated between the true model and the resistivity model, and normalized

Downloaded from academic.oup.com/gji/article/247/3/gga402/8853762 by guest on 16 November 2026

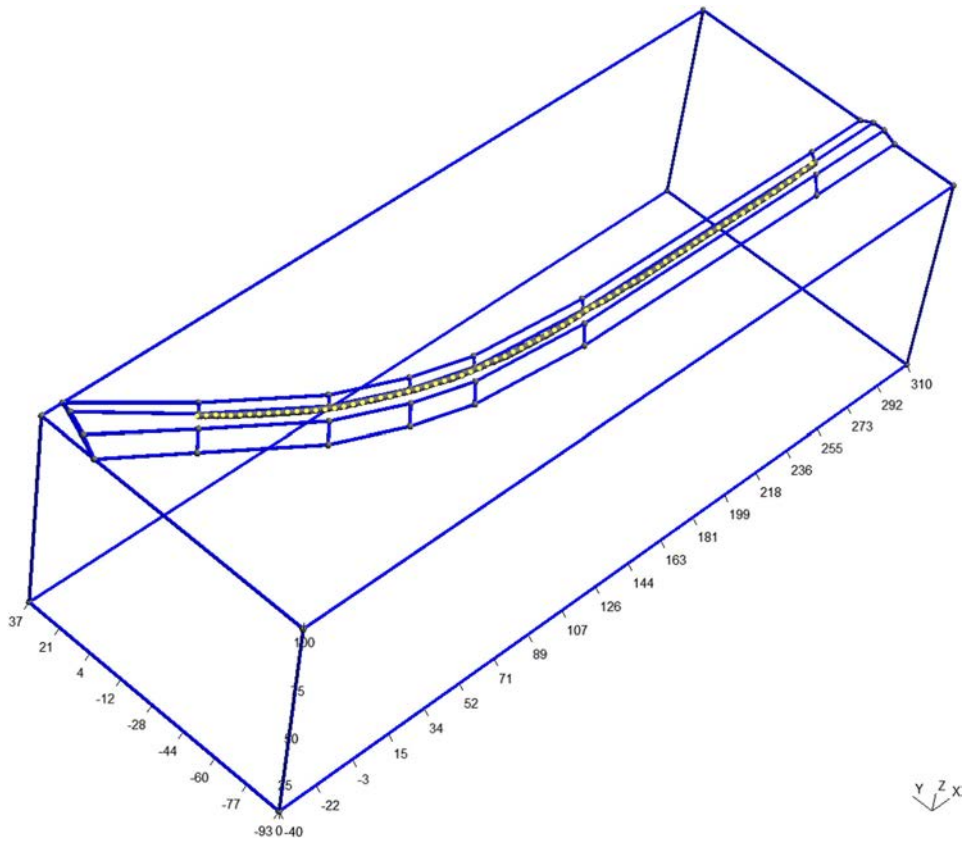


Figure 8. The 3-D model of the embankment created in Gmsh for the inversion of ERT field data. The dots on the crest represent the electrodes of the ERT line. The origin of the axes ($[X, Y, Z] = [0, 0, 0]$) is in the first electrode of the ERT line.

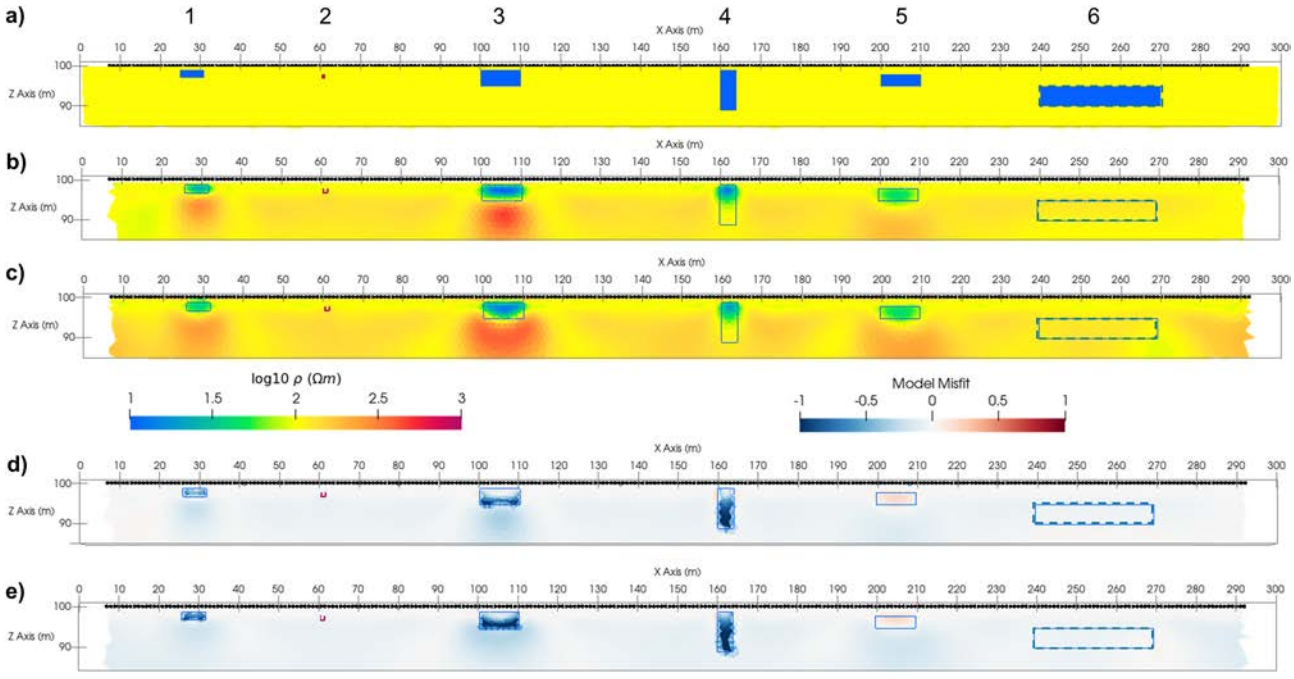


Figure 9. (a) The section of the true synthetic model S1 including all the anomalies. The results from 2-D inversion of (b) DD data and (c) WS data. The model misfit with respect to the true model for the (d) DD and (e) WS data.

Downloaded from academic.oup.com/gji/article/247/3/ggag402/8853762 by guest on 16 November 2026

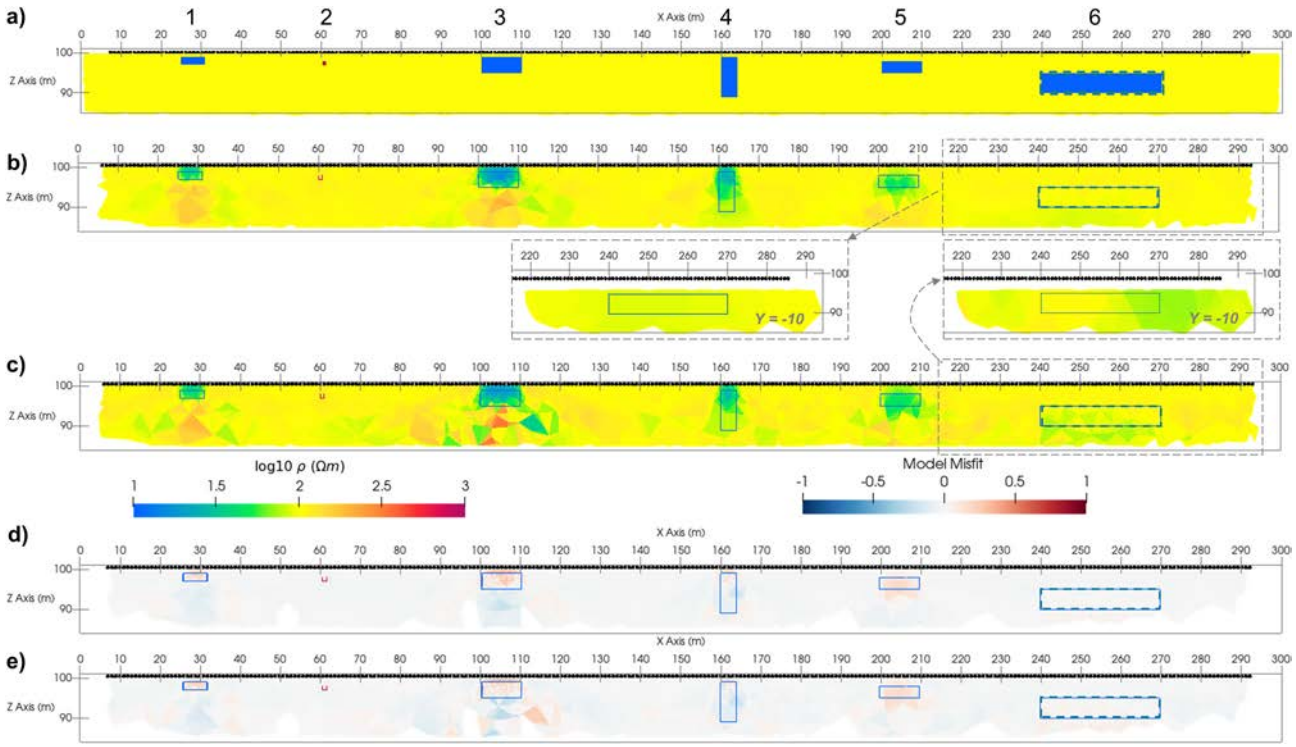


Figure 10. The section below the electrodes of: (a) the true synthetic model S1 including all the anomalies; (b) the result from 3-D inversion of DD data; (c) the result from 3-D inversion of WS data; (d) model misfit for DD data; (e) model misfit for WS data. The subpanels in panels (b) and (c) are the slices at $Y = -10$ to inspect anomaly no. 6.

Table 1. Computation requirements and outputs for 2-D and 3-D inversion of model S1.

Inversion	Data	Total memory required (GB)	Runtime	Iterations	RMSE
2-D	DD	1.4	3’	1	1.13
	WS	2.4	9’	1	1.0
3-D	DD	10	32’	1	0.61
	WS	6	4 hr	1	1.17

with respect to the true model. The calculation considered the resistivity value in log scale and was performed, for each tetrahedron of the 3-D models, through the formula: [(true model)—(resistivity model)]/true model. The calculation of the model misfit for the 2-D results (Fig. 9) adopted as true model the vertical 2-D section below the electrode line from the true 3-D model. Since the mesh of 2-D inversion was different from the mesh of 3-D forward modelling, a resampling was carried out in Paraview from the fine mesh used for forward modelling to the coarse mesh of the 2-D inverse model. The model misfit was not only calculated for the visualization in panels (d) and (e) of Figs 9 and 10, but also inspected at each anomaly to better quantify the validity of the inversion results. In the volume of the model misfit, we isolated the box volume corresponding to each anomaly plus a buffer surrounding layer of 1 m to incorporate all the tetrahedra of the anomaly. Then, we extracted the mean value of the model misfit inside each anomaly by using the filter ‘Descriptive Statistics’ and the ‘spreadsheet view’ in Paraview.

Table 1 lists some general information about the computation requirements (total memory) and final outputs (total runtime, number of iterations and final root mean square error (RMSE)) to run 2-D and 3-D inversions of DD and WS data from S1 model. As expected, 3-D inversion was more computationally expensive than 2-D inversion.

The models in Figs 9(b) and (c) and 10(b) and (c) adequately reproduce the anomalies no. 1, 3, 4, 5, after both 2-D and 3-D inversions, while anomalies nos. 2 and 6 were not identified due to their challenging features for ERT modelling in the chosen domain. Anomaly no. 2 is a small transversally elongated body with a resistivity one order of magnitude higher than the background, while anomaly no. 6 is a thin slab far and eccentric with respect to the electrode line with a resistivity two orders of magnitude less than the background. The main difference between the 2-D and 3-D results is that the models from 2-D inversion (Figs 9b and c) show stronger resistive artefacts below anomalies nos. 1, 3 and 5 than in the 3-D results (Figs 10b and c). The vertical shape of anomaly no. 4 and the homogeneous 100-Ωm background are better characterized in the 3-D sections than in the 2-D models, that were negatively affected because 3-D features were solved as varying only in two dimensions (N.G. Papadopoulos *et al.* 2007). The narrow eccentric anomaly no. 6 is always scarcely identified because it does not belong to the extracted slice below the electrodes, but it is worth noting that the 3-D results present a resistivity decrease with depth as an effect of the presence of 3-D body no. 6 (Figs 10b and c). An advantage of 3-D inversion

Downloaded from academic.oup.com/gji/article/247/3/ggag402/8853762 by guest on 16 November 2026

Table 2. The model misfit of each anomaly for the results after 2-D and 3-D inversion of model S1 with both DD and WS data. The mean value of the model misfit was calculated inside each anomaly in Paraview. The model misfit among the six anomalies is reported in the last row and is the mean of the absolute values of the six misfits.

Anomaly no.	S1 model misfit (mean values)			
	2-D		3-D	
	DD	WS	DD	WS
1	−1.90E−01	−2.47E−01	1.50E−02	5.00E−03
2	−1.40E−02	−3.40E−03	−1.60E−02	−1.80E−02
3	−1.85E−01	−2.33E−01	8.10E−02	7.40E−02
4	−2.48E−01	−2.77E−01	4.10E−02	1.80E−02
5	8.38E−02	8.76E−02	−7.20E−02	−6.60E−02
6	n.a.	n.a.	−5.10E−02	−4.60E−02
Mean (abs)	1.44E−01	1.70E−01	4.60E−02	3.78E−02

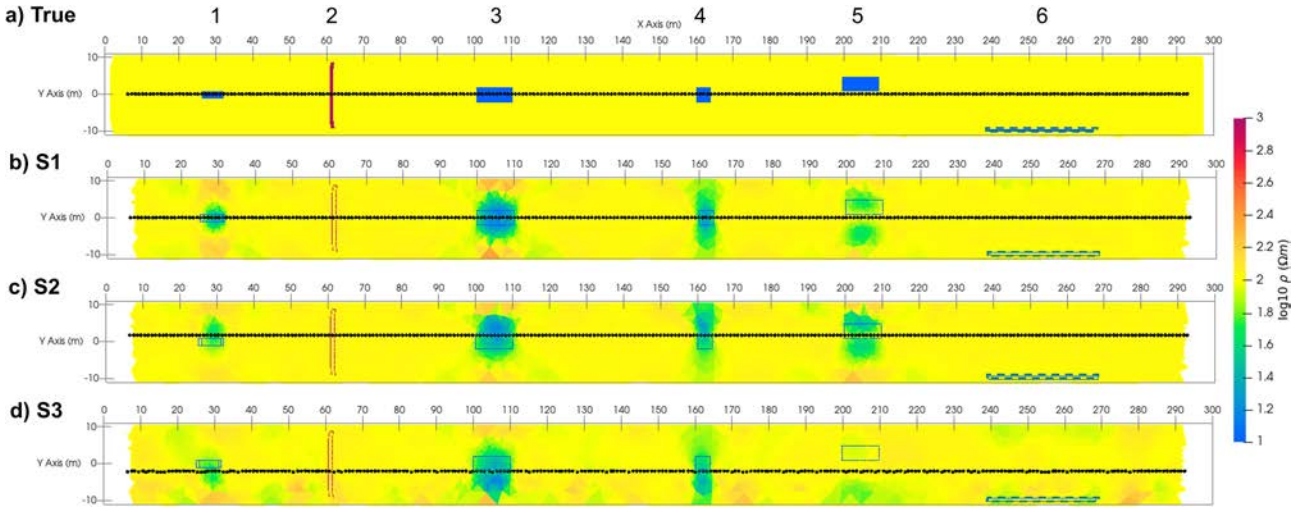


Figure 11. Top view of the embankment body (between $Y = -10$ and 10 m) at 2 m of depth below the crest of the embankment: (a) true straight model with the resistivity anomalies; resistivity model after 3-D inversion of DD data for (b) S1, (c) S2 and (d) S3 models.

is that the lateral extension (in the *Y*-axis direction) of the subsurface structures can be inspected, even in low sensitivity portions, as in the case of anomalies nos. 5 and 6. The dashed subpanels in Figs 10(b) and (c) represent the vertical slice crossing anomaly no. 6 (at $Y = -10$ m) and depict a conductive region. Finally, the model misfit in Figs 9(d) and (e) and 10(d) and (e) quantitatively depicts the closeness of the final models to the true model and shows that the 3-D results had lower misfit than the 2-D results for the anomaly detection and resistivity value.

It could be observed that the mesh for 2-D inversion is finer than that for 3-D inversion below the electrodes. This was justified by the high number of nodes of the tetrahedral mesh which must be restrained for the 3-D computation. To improve the comparison between 2-D and 3-D results, we carried out a 2-D inversion test with a mesh coarser than that shown in Fig. 9 and composed of a number of nodes similar to those of the section in Fig. 10, that is, 3500 nodes (instead of 5700). The resulting 2-D models (not shown here) were similar to those in Fig. 9 and presented high-contrast artefacts and a heterogeneous background that hence were not influenced by the parametrization or smoothing of the 2-D inversion.

Table 2 lists the values of the model misfit for model S1, after 2-D and 3-D inversion of both DD and WS data. At the scale of the localized anomalies, the model misfit was higher (in absolute value) in the 2-D results than in the 3-D results (except for anomalies nos. 2 and 5), while in the 3-D results the model misfit was higher in DD data than in WS data (except for anomaly no. 2). Anomaly no. 6 is not part of the 2-D section so its model misfit could not be calculated in the 2-D result. The model misfit among the six anomalies in the last row of Table 2 was calculated as the mean of the absolute values of the six anomaly misfits. This absolute error metric was adopted for only the mean misfit to avoid cancellation between the positive and negative misfits of the six anomalies. The lowest value among the mean misfits is for the 3-D results.

5.2 *Comparison among S1, S2, S3 models*

As previously explained, the S1, S2 and S3 models had different locations of the electrode line. Fig. 11 illustrates the top view (*XY* plane) of the embankment body (between $Y = -10$ and 10 m) from 2 m of depth below the crest of the embankment. The true model with the correct location of the anomalies is shown in Fig. 11(a). The results for DD data are shown in Figs 11(b), (c) and (d) for S1, S2

Downloaded from academic.oup.com/gji/article/247/3/ggag402/8853762 by guest on 16 November 2026

Table 3. The model misfit of each anomaly for the results after 3-D inversion of models S1, S2 and S3 with DD data. The mean value of the model misfit was calculated inside each anomaly in Paraview. The model misfit among the six anomalies is reported in the last row and is the mean of the absolute values of the six misfits.

Anomaly no.	Model misfit for DD (mean values)		
	S1 model	S2 model	S3 model
1	1.50E−02	2.17E−02	2.20E−02
2	−1.60E−02	−1.70E−02	−7.60E−02
3	8.10E−02	9.99E−02	−4.29E−01
4	4.10E−02	5.90E−02	6.50E−02
5	−7.20E−02	−1.10E−02	−9.10E−02
6	−5.10E−02	−5.80E−02	−4.30E−02
Mean (abs)	4.60E−02	4.44E−02	1.21E−01

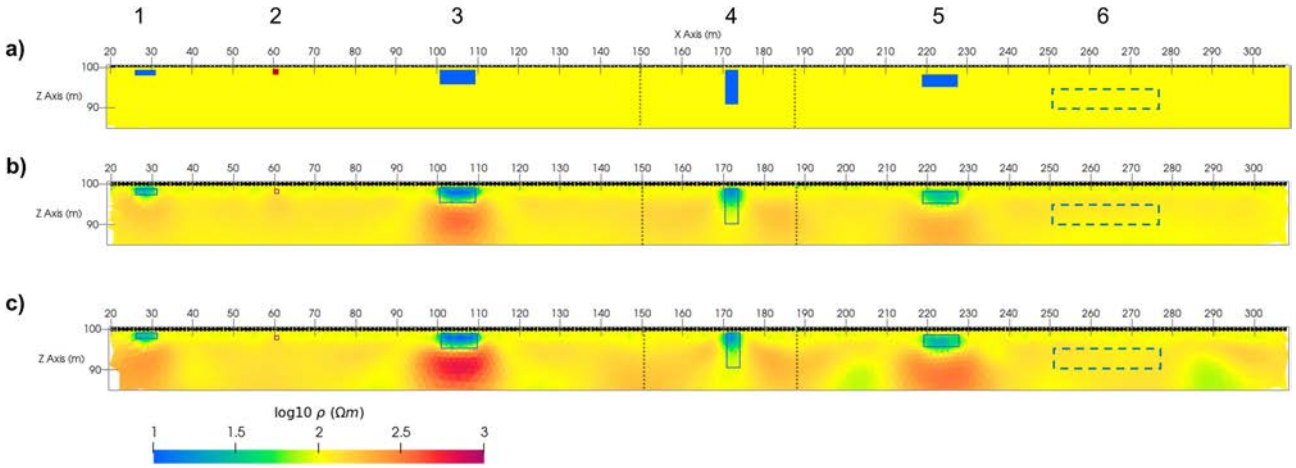


Figure 12. (a) The section of the true synthetic model C1 including all the anomalies. The results for C1 model from 2-D inversion of (b) DD and (c) WS data. The vertical dotted lines represent the corners where the model curves.

and S3 models, respectively. For WS data, the results are in Appendix D (Supplementary Material). The resistivity anomalies are better characterized if the ERT line passes exactly above them, in the high-sensitivity region. In fact, anomalies nos. 1, 3 and 4 are correctly identified in model S1 (Fig. 11b), while in models S2 and S3 the resistivity corresponding to them is slightly shifted towards the ERT line. Anomaly no. 5 is acceptably characterized in model S1 (Fig. 11b), even if it is not centred in $Y = 0$, is properly characterized in model S2 (Fig. 11c), because it wholly lies below the shifted ERT line, and is not nearly seen in model S3 (Fig. 11d), because it is too far from the electrodes. To quantify the appropriateness of the results, Table 3 lists the mean value of the model misfit inside each anomaly for the 3-D models S1, S2 and S3, after 3-D inversion of DD data. The lowest value of model misfit (in absolute value) is in model S1 for anomalies 1 to 4, because they are centred in $Y = 0$. The lowest model misfit for anomaly no. 5 is in model S2, because it is shifted towards $Y = 2$ m. The lowest model misfit for anomaly no. 6 is in model S3, because it is shifted towards $Y = -2$ m. Therefore, the buried features that are not exactly below the ERT line are imperfectly identified. As well as the closeness of the anomalies to the ERT line, another possible reason of the transversal shift of the resistivity distribution could be the closeness of the electrodes to the boundary of the slope of the embankment, that may amplify the resistivity anomaly. It is worth noting that the anomaly identification is centred in the exact position for S1 result, but asymmetric towards the ERT line for S2 and S3 results. This may be owed to the equivalence of the solutions and the lack of data coverage in the transversal direction. The model misfit for models S2 and S3 is shown in Appendix D (Supplementary Material).

5.3 *Results for C1 model*

The synthetic data from the curved model C1 were inverted and the results are shown in Figs 12 and 13 for 2-D and 3-D models, respectively.

Table 4 lists the computation requirements (total memory) and final outputs (total runtime, number of iterations and final RMSE) to run 2-D and 3-D inversion of DD and WS data from C1 model.

The true model is represented in Fig. 12(a) with a 2-D projection of the curved model C1 so that the electrodes are still 1m-spaced. Anomaly no. 6 is represented with a dashed line because it is not exactly below the ERT line. The 2-D resistivity models are shown in

Downloaded from academic.oup.com/gji/article/247/3/ggag402/8853762 by guest on 16 November 2026

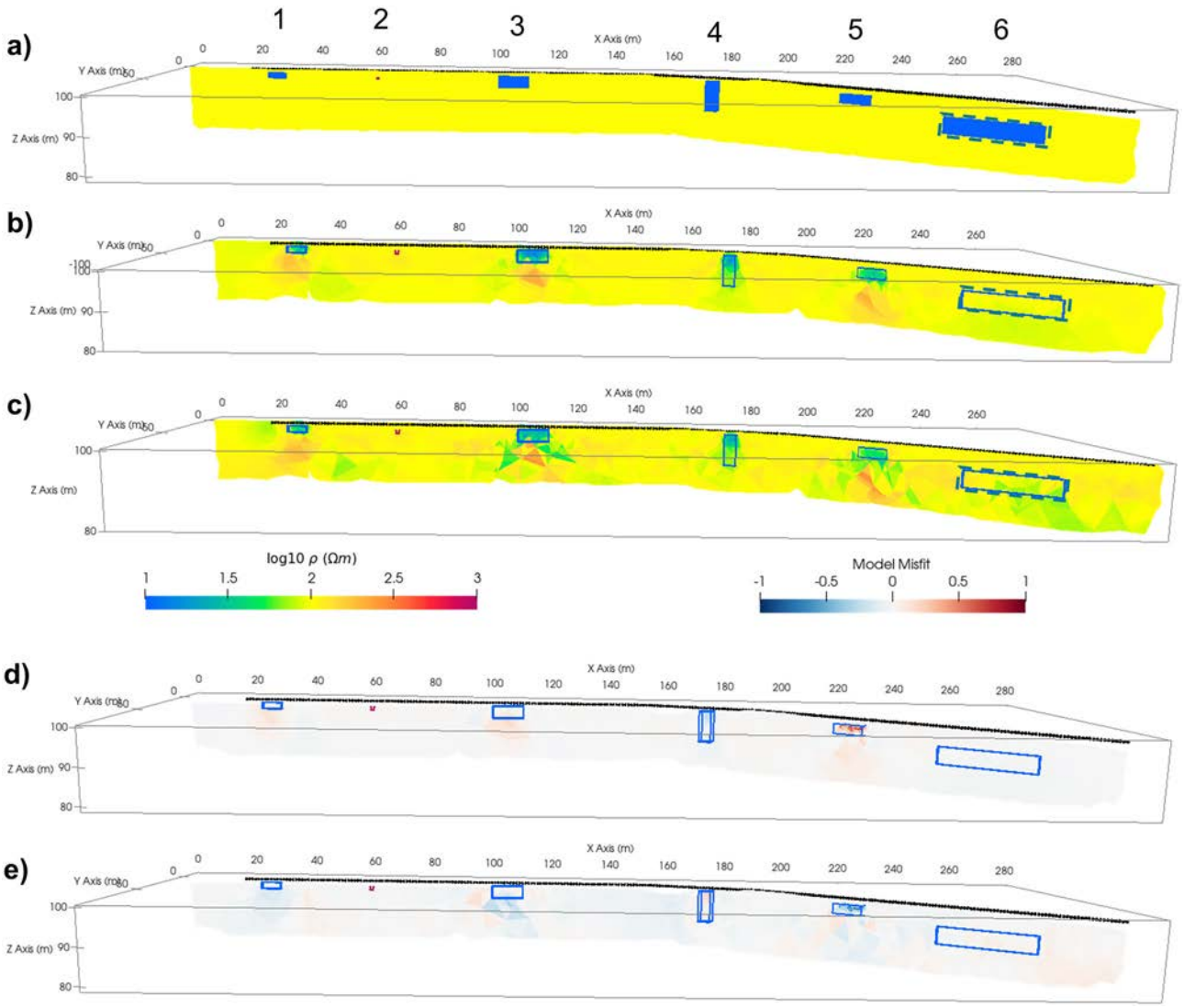


Figure 13. The section below the electrodes of: (a) the curved synthetic model C1 including all the anomalies; (b) the result from 3-D inversion of DD data; (c) the result from 3-D inversion of WS data; (d) model misfit for DD data; (e) model misfit for WS data.

Table 4. Computation requirements and outputs for 2-D and 3-D inversion of model C1.

Inversion	Data	Total memory required (GB)	Runtime	Iterations	RMSE
2-D	DD	1.4	13’	2	1.0
	WS	2.4	18’	3	1.0
3-D	DD	14	54’	1	0.62
	WS	14	6 hr	1	1.18

Figs 12(b) and (c) for DD and WS data, respectively. The vertical dotted lines at $X = 150$ m and $X = 188$ m represent the position of the corners in the curved model. The anomalies in the oblique branch (nos. 4, 5 and 6) are not in the same horizontal coordinate as in the 3-D model (Fig. 3) due to the projection of the curved branch, but they are placed at the same electrode number as in the 3-D model C1. Both DD and WS models present a good identification of anomalies nos. 1, 3, 4 and 5, as in the straight model (Fig. 9). The curves did not seem to significantly affect the results, which are highly similar to those of the straight model in terms of anomaly identification, while the values of the background resistivity are worse than in the straight model (Fig. 9). The whole model misfit with respect to the true model was not calculated because the 3-D model, which is curved, could not be compared cell-by-cell with a 2-D model that is projected and flat. The comparison between the 2-D results and the true model is shown in Fig. 12 through the edges of the anomalies of the true model that are overlapped to the results. The model misfit of the 2-D results was calculated for each anomaly by dividing the true model C1 into two portions: the straight branch and the oblique branch. For anomalies nos. 1–3 in the straight branch, the model misfit was calculated as for model S1, since their positions coincide. The model misfit of the anomalies in the oblique branch was calculated by rotating the oblique portion of C1 on the 2-D result. The values of the model misfit for the anomalies in the 2-D

Downloaded from academic.oup.com/gji/article/247/3/ggag402/8853762 by guest on 16 November 2026

Table 5. The model misfit of each anomaly for the results after 2-D and 3-D inversion of model C1 with both DD and WS data. The mean value of the model misfit was calculated inside each anomaly in Paraview. The model misfit among the six anomalies is reported in the last row and is the mean of the absolute values of the six misfits.

Anomaly no.	C1 model misfit (mean values)			
	2-D		3-D	
	DD	WS	DD	WS
1	−1.38E−01	−7.20E−01	−2.00E−02	1.60E−02
2	−4.80E−02	−5.00E−02	1.80E−02	−1.70E−02
3	−2.78E−01	−2.76E−01	−7.20E−02	6.40E−02
4	1.07E−01	1.00E−01	−5.30E−02	3.12E−02
5	−4.41E−01	−3.90E−01	1.60E−02	−1.20E−02
6	n.a.	n.a.	4.50E−02	−4.60E−01
Mean (abs)	2.02E−01	3.07E−01	3.73E−02	1.00E−01

results of DD and WS data are reported in Table 5. By comparing the 2-D results from S1 model (Table 2) and from C1 model (Table 5), the highest model misfit (in absolute value) is mostly in C1 for DD (60 per cent of anomalies) and WS data (80 per cent of anomalies). Moreover, anomaly no. 5 has a higher misfit in the 2-D results from C1 than in those from S1, thus suggesting that assuming a curved line as a planar one may worsen the model misfit.

Fig. 13(a) shows the 3-D volume below the ERT line extracted from the true model, while Figs 13(b) and (c) show the inversion results for DD and WS data, respectively. The inversion results correctly locate the resistivity anomalies nos. 1, 3, 4 and 5. Anomaly no. 6, despite far and deep, has an influence on the model, with a resistivity decrease. Figs 13(d) and (e) depict the model misfit with respect to the true model calculated as for model S1 (Fig. 10). Table 5 reports the mean values of the model misfit inside each anomaly for the 3-D inversion of model C1 for both DD and WS data. The low values of the model misfit confirm the good correspondence to the true model. For the 3-D results, the misfit values of WS results are (in absolute value) slightly lower than those of DD results. The misfit of the 3-D results is always an order of magnitude lower than those of the 2-D results. The mean values among all the anomalies (last row of Table 5) are lower for the 3-D results, as happened for model S1 (Table 2). However, the comparison between the mean misfits of models S1 and C1 indicates that for the 2-D results the lowest misfits are for S1, while for the 3-D results the mean misfits are all around 4.E−02 except for the WS data of the C1 model (where anomaly no. 6 contributes to the high misfit).

5.4 *Results for C2 and C3 models*

The results for models C2 and C3 were highly similar to those of model C1 in terms of final RMSE and total runtime. The only difference with respect to model C1 is the position of anomaly no. 4, which changes corner of the curved model (see Fig. 3a).

Fig. 14 displays the results from 2-D inversion of DD data for models C2 and C3. The WS results are shown in Appendix D (Supplementary Material). Figs 14(a) and (c) show the true models C2 and C3, respectively. Figs 14(b) and (d) show the 2-D resistivity models for C2 and C3, respectively. The identification of anomaly no. 4 in Figs 14(b) and (d) is correct despite the position in the corner of the curved model.

Fig. 15 is the analogous of Fig. 14 but for the 3-D result. There is a substantial correspondence between the true model and the inverted models, for both C2 and C3. The vertical shape of anomaly no. 4 is better characterized in the 3-D models (Fig. 15) rather than in the 2-D models (Fig. 14). In the 2-D inversion results, below the conductive anomalies nos. 1, 3 and 5, there is a strong resistive artefact, as happened for model S1 (Fig. 9) and C1 (Fig. 12). The model misfit for C2 and C3 is shown in Appendix D (Supplementary Material).

6 RESULTS FROM FIELD DATA

2-D and 3-D inversions of field data were initialized by a homogeneous starting model of 100 Ωm, as usually employed in ERT modelling (A. Binley 2023). Although from both the geological scheme (Fig. 6c) and the data (Fig. 7) we expected a resistivity variation with depth, a heterogeneous (or layered) starting model would have negatively constrained the result. The homogeneous starting model of 100 Ωm was the default in ResIPy and ensured that all the inversion tests converged in few iterations with low final RMSEs. The topography was not included because the embankment crest was essentially flat. 3-D inversion was performed on a model including the true embankment geometry, as explained in Section 4. Table 6 lists the computation requirements (total memory) and final outputs (total runtime, number of iterations and final RMSE) to run 2-D and 3-D inversion of field data. In this Section, the term 'conductive' refers to resistivity values less than 70 Ωm ($\log_{10}\rho < 1.8$ Ωm), while the term 'resistive' refers to resistivity values higher than 400 Ωm ($\log_{10}\rho > 2.6$ Ωm).

A posterior analysis of the resistivity models is usually carried out due to inherent non-uniqueness of the inverse solution. To appraise the inversion results it is possible to calculate the sensitivity function (M.H. Loke 2004), that gives insight into how much

Downloaded from academic.oup.com/gji/article/247/3/ggag402/8853762 by guest on 16 November 2026

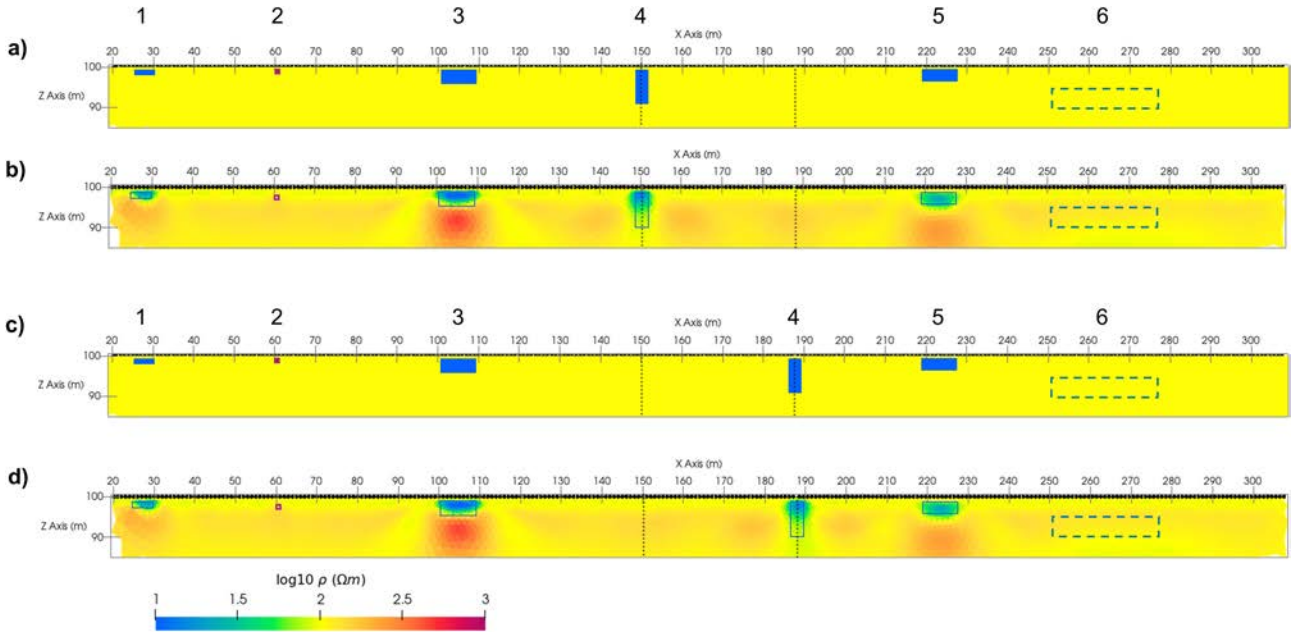


Figure 14. (a) The section of true model C2; (b) 2-D inversion of DD data for C2; (c) the section of true model C3; (d) 2-D inversion of DD data for C3. The vertical dotted lines represent the corners where the model curves.

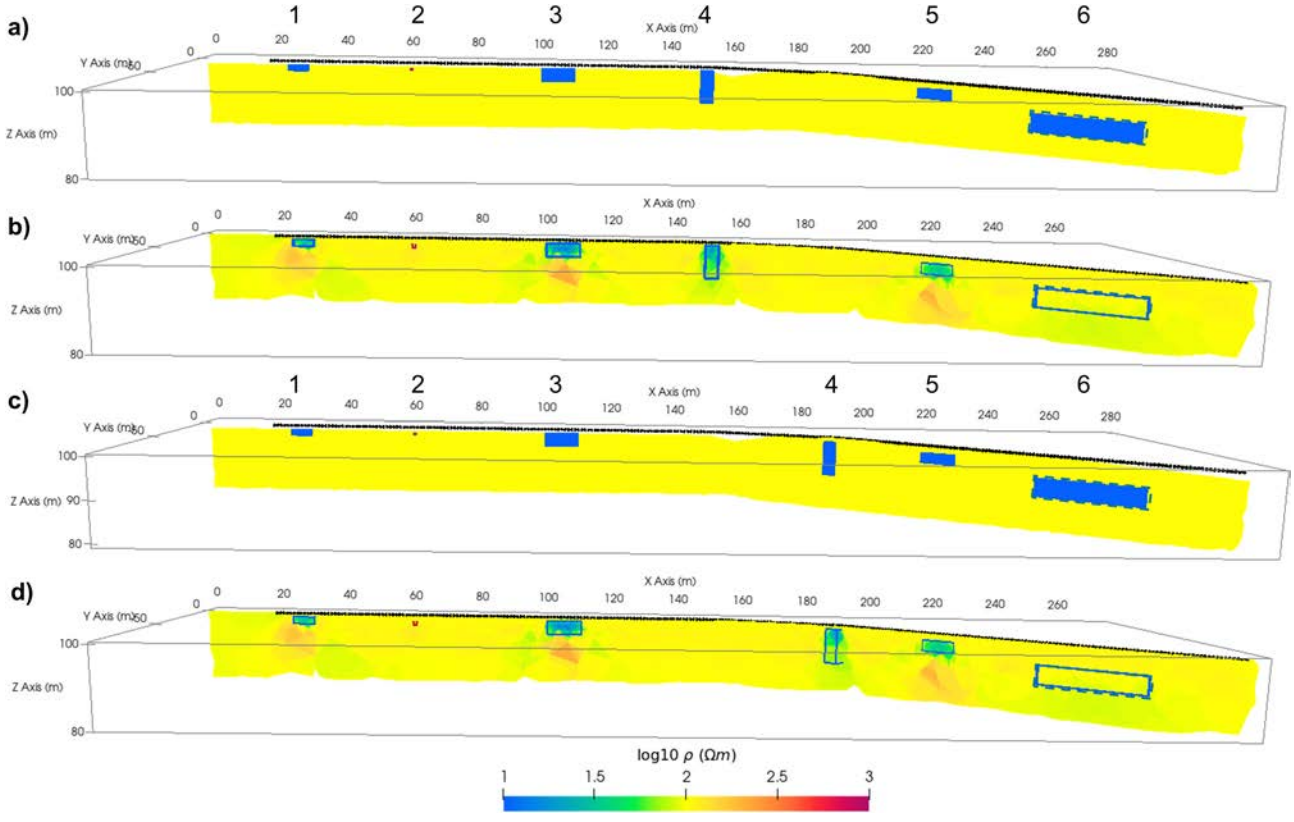


Figure 15. (a) 3-D section of true model C2; (b) 3-D inversion of DD data for C2; (c) 3-D section of true model C3; (d) 3-D inversion of DD data for C3.

Table 6. Computation requirements and outputs for 2-D and 3-D inversion of field data.

Inversion	Data	Total memory required (GB)	Runtime	Iterations	RMSE
2-D	DD	1.3	52’	9	1.43
	WS	2.3	50’	7	1.0
3-D	DD	13	8 hr	2	1.08
	WS	16	17 hr	2	1.42

Downloaded from academic.oup.com/gji/article/247/3/ggag402/8853762 by guest on 16 November 2026

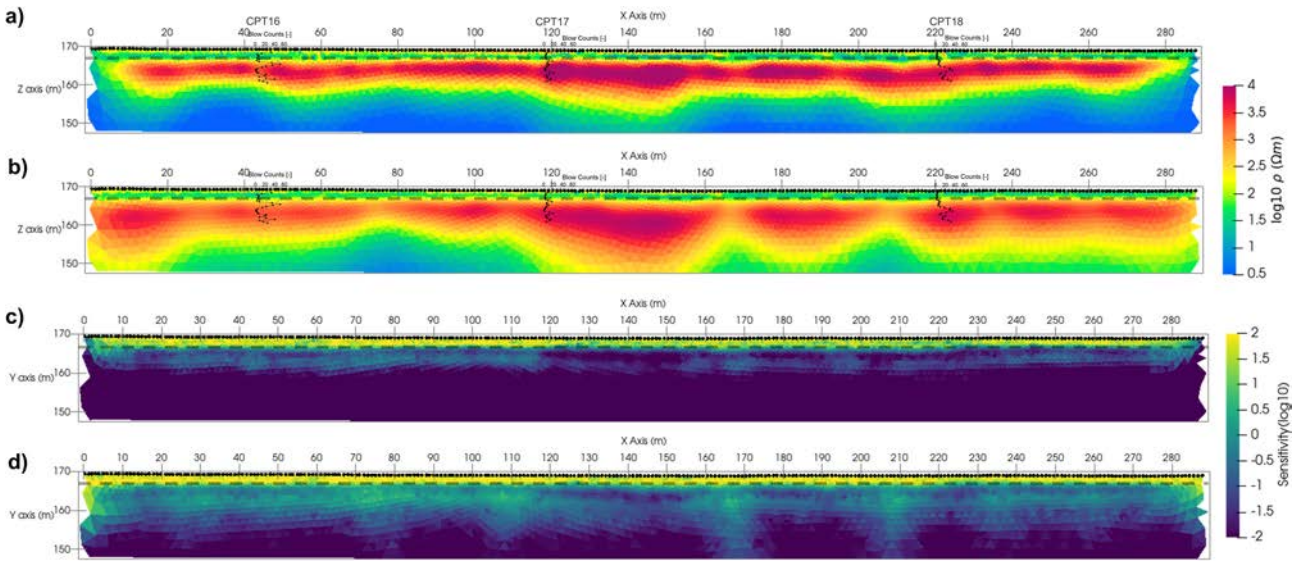


Figure 16. Results after 2-D inversion of field data from the Verolengo embankment: resistivity models with the three SCPTs for (a) DD and (b) WS data; sensitivity map for the resistivity models of (c) DD and (d) WS data. The dashed line at 3 m of depth represents the base of the embankment.

the resulting resistivity of the model reflects the data (M.H. Loke *et al.* 2013). In ResIPy, the sensitivity map is calculated according to A. Binley & A. Kemna (2005) and is computed at the end of the inversion if the inversion setting called 'resolution matrix = 1' is selected (M.H. Loke 2004). The sensitivity map is stored in the output file 'f001_sen.dat' of the ResIPy project. In a section of the sensitivity map, the higher the sensitivity value, the more reliable is the resistivity value. Generally, the sensitivity is high close to the electrodes and the surface, while it decreases with depth and distance from the ERT line. In the following sections, the resistivity models are shown together with the sensitivity map.

6.1. *Two-dimensional inversion of field data*

The resistivity models are shown in Figs 16(a) and (b) for DD and WS data, respectively. In both models, there is a shallow 3m-thick conductive layer corresponding to the embankment body, above the dashed grey line. The resistivity distribution in the core of the embankment appears quite homogeneous, without abrupt variations. At $X = 164$ m there is a mild lateral discontinuity derived from the lot division during the construction site. Below it, there is a high-resistivity layer (up to 10^4 Ωm) that has a minimum thickness of around 6 m. In both models, the resistive layer does not seem continuous and becomes thin at $X = 75$, 110, 164 and 210 m. The little differences between the two models are owed to the optimal horizontal resolution of the DD configuration that enhances lateral variations, while the WS configurations enhance horizontal stratifications that are marked for this embankment. The resistivity models are overlapped with the blow counts of the three SCPTs (CPT16, CPT17 and CPT18). The sensitivity map of these results is provided in Figs 16(c) and (d) for DD and WS models, respectively. The maximum value of sensitivity (in yellow) lies inside the embankment (i.e. our investigation target), as expected with an electrode spacing of 1 m. Below the embankment, the sensitivity gradually decreases and nullifies at around 10 m of depth.

6.2. *Three-dimensional inversion of field data*

The results of 3-D inversion are depicted in Figs 17(a) and (b) for the slice below the electrodes for DD and WS data, respectively. The dashed line represents the base of the embankment, while the three SCPTs are overlapped to the resistivity models. Figs 17(c) and (d) show the sensitivity map of the vertical slice for DD and WS models, respectively.

The shallow conductive layer is clear in the straight branch ($X > 140$ m), while it is discontinuous at $X < 140$ m. This conductive layer is thicker than the corresponding one in the 2-D model, probably thanks to the inclusion of the true 3-D geometry. There is an evident discontinuity in the shallow conductive layer at $X = 150$ m (electrode no. 164), which exactly corresponds to the lot division of the construction site (see Fig. 6c). This contrast is less evident in the 2-D results (Fig. 16), where it happens at around $X = 164$ m (electrode no. 164) due to the projection of the coordinates of the curve. The resistive layer (>400 Ωm) is between 10 and 20 m thick, and it is close to the surface at $X = 70-90$ m. Moreover, the resistivity of the resistive layer is less than that of the 2-D models, which is explained by the 3-D inversion modelling that often smooths the resistivity values due to the distribution of the total resistance in the transversal direction. The sensitivity in Figs 17(c) and (d) has positive values inside and slightly below the embankment, while it becomes negative below 10 m of depth, that is beyond the maximum investigation depth.

Downloaded from academic.oup.com/gji/article/247/3/ggag402/8853762 by guest on 16 November 2026

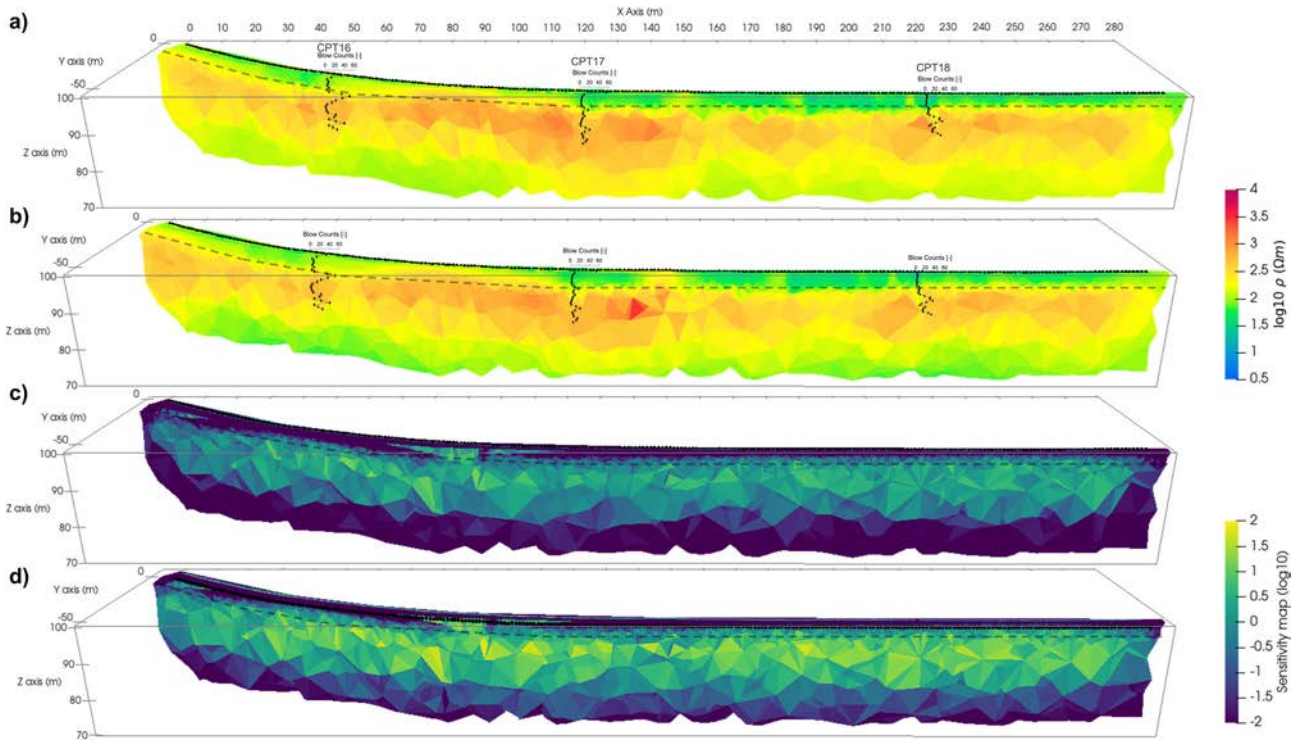


Figure 17. Results after 3-D inversion of field data from the Verolengo embankment. Sections below the electrodes from the 3-D model for: resistivity with the three SCPTs for (a) DD and (b) WS data; sensitivity map for (c) DD and (d) WS data. The dashed grey line represents the base of the embankment.

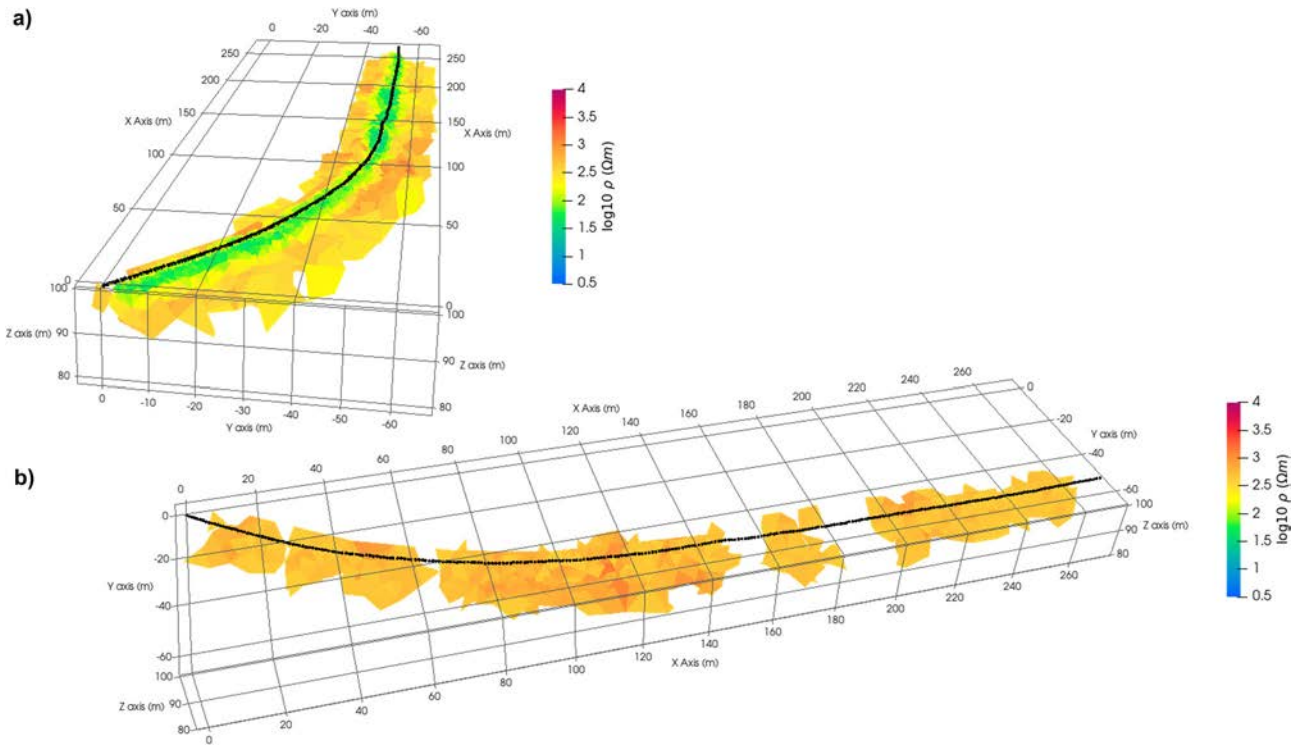


Figure 18. The resistivity model after 3-D inversion of DD data from the Verolengo embankment: (a) portion of the 3-D resistivity model having a sensitivity > 0; (b) portion of the 3-D resistivity model having $\rho > 400$ Ωm and sensitivity > 0.

Further considerations can be pointed out from the comparison between the resistivity models and the geotechnical data of the SCPTs. The blow counts of CPT16 and CPT18 abruptly increase in coincidence of the top of the resistive layer, while it is less evident in CPT17, that has a maximum of 20 blow counts at 3 m of depth where the resistivity increase.

Fig. 18 shows selected portions of the 3-D resistivity model, after inversion of DD data. Fig. 18(a) depicts the subvolume with

Downloaded from academic.oup.com/gji/article/247/3/ggag402/8853762 by guest on 16 November 2026

positive sensitivity and highlights that the resistive layer extends below the embankment not only with depth but also transversally, with acceptable level of confidence. Fig. 18(b) depicts the subvolume with sensitivity above zero and resistivity higher than 400 Ωm, which is reasonable for a sandy soil with gravel (J.M. Reynolds 2011). The selected volume highlights that the resistive layer below the embankment is clearly interrupted at $X = 65$, 150 and 190 m. Such evidence would not have been possible from a 2-D result.

7 DISCUSSION

The results shown in the previous sections clearly demonstrate that the 3-D results outperform the 2-D results for the characterization of the anomalies inside an embankment, even with a 2-D data set and a curved line. For the synthetic data, this was evident from the comparison with the true model and from the calculation of the model misfit. For the field data, the 3-D results were more coherent than the 2-D results with the known geology and geotechnical data.

The main considerations that arise from our results are:

(i) 2-D inversion is an adequate approach in presence of shallow anomalies close to the electrodes, simple and blocky geometry of the model domain and non-curved ERT lines. Otherwise, 3-D inversion is preferable.

(ii) 2-D inversion is negatively affected by both the three-dimensionality of the buried features and the 3-D effects of the peculiar geometry of the embankment. This had already been pointed out for archaeological targets, but with 3-D blocky geometry (N.G. Papadopoulos *et al.* 2007), and for the embankments, but without the comparison with 3-D inversion results (A. Hojat *et al.* 2020). From our synthetic results in Figs 9(b) and (c), the 2-D models present conductive artefacts (green) in the upper 3 m of depth corresponding to the embankment and some high resistivity (reddish) artefacts in the basement. These artefacts are not visible in the 3-D results (Fig. 10). Another negative effect of the peculiar geometry of the embankment on the 2-D results can be seen in the background resistivity of the models in Fig. 9, that is more resistive and less homogeneous than in the 3-D results. This outcome was proved by the calculation of the model misfit for each anomaly after 2-D and 3-D inversion (Table 2). The highest misfit was found in the 2-D results and was in most cases an order of magnitude higher than in the 3-D results.

(iii) The shape and resistivity of the subsurface anomalies of the synthetic models are better identified in *X*- and *Z*-directions if 3-D inversion is performed (see Figs 9 and 10). The 2-D results showed artefacts because the 3-D anomalies were solved as varying in only two dimensions.

(iv) 2-D inversion does not allow any inference about eccentric or far anomalies that can be inspected transversally only in 3-D (see Figs 9, 10 and 18). While 2-D inversion produces a satisfactory model (Fig. 9), 3-D inversion offers the opportunity of analysing in a volume the presence of eccentric bodies that are far from the electrode line and sightly influence the 3-D results (see subpanels for anomaly no. 6 in Fig. 10). The synthetic examples demonstrated that the eccentric/far anomalies are detected only after 3-D inversion. The field example demonstrated that a single 2-D line inverted in 3-D provides good values of sensitivity not only exactly below the line but also transversally. The volume extracted in Fig. 18 from the sensitivity map highlights this finding, which can be more useful than a 2-D model for posterior interpretation.

(v) In the straight synthetic model, the vertical shape of anomaly no. 4 is better characterized in 3-D than in 2-D (Figs 9 and 10), with a vertically elongated conductive region highly similar to the true shape of the anomaly (and with low values of model misfit as in Table 2). The analysis of the sensitivity map of the inversion results may explain this outcome: The sensitivity map has higher values in the 3-D section than in the 2-D model (not shown here).

(vi) The 3-D approach allows the true curvature of the ERT line to be included in the modelling, thus avoiding the projection of the resistivity distribution section on a flat surface, as happens with 2-D inversion (see Figs 12–15). We calculated the model misfit for each anomaly inside the straight model S1 (Table 2) and the curved model C1 (Table 5) and proved that for most of the anomalies the misfit is worse in the 2-D results than in the 3-D results. The misfit also worsens in a 2-D assumption of a curved ERT line (i.e. in the 2-D inversion of the curved C1 model). The 3-D model should reproduce the peculiar geometry of the embankment, including the lateral slopes or possible curves to avoid geometrical simplifications (see Figs 13, 15 and 17). This may seem obvious, but for field data a flat blocky 3-D model disregarding the specific geometry of the embankment (not shown here) gave a resistivity distribution that was less conform to the known geology and more heterogeneous than that of the 3-D model with the true geometry.

(vii) Regarding the position of the ERT line with respect to the buried anomalies and the edges of the embankment crest, the sections of the 3-D models in Fig. 11 suggest that the anomaly position is always correctly identified along the *X*- and *Z*-directions, while the transversal location (*Y*-direction) seems shifted towards the position of the ERT line. Table 3 reports the lowest model misfit for the buried anomalies that are exactly below the ERT line, while the model misfit worsens if their distance from the ERT line increases. The sensitivity analysis with the shift of the ERT line (S1, S2 and S3 models) shows that the resistivity distribution seems biased towards the ERT line, thus suggesting that the exact transversal boundaries of the anomalies may not be univocally determined. This issue can be related to the equivalence of the inverse problem solutions and the lack of data coverage in the transversal direction. To improve that, it would be appropriate to acquire additional ERT lines longitudinally on the crest or transversally on the slopes of the embankment, thus achieving a full 3-D approach.

(viii) Regarding the field data example, the resistivity distribution from the 2-D and 3-D results shows horizontally layered features without abrupt discontinuities or anomalous bodies at depth. There is evidence of the lot division of the construction site in a shallow

Downloaded from academic.oup.com/gji/article/247/3/ggag402/8853762 by guest on 16 November 2026

lateral discontinuity in the embankment at electrode no. 164, that is, at $X = 164$ m in the 2-D models (Fig. 16) and more evident at $X = 150$ m in the 3-D models (Fig. 17). The comparison between the 2-D and 3-D results suggests that the 2-D model enhanced the resistivity contrasts and might have overestimated the resistivity of the resistive layer, that is, 10^4 Ωm in contrast to 10^3 Ωm obtained in the 3-D models. The resistivity of the 3-D results is in line with the known geology of the embankment shown in Fig. 6(c). The shallow conductive layer is 3 m thick, that exactly corresponds to the new clayey backfill material used during the construction site in 2023. The underlying resistive region corresponds to the ground level composed of gravel and pebbles in a silty–sandy formation, which justifies a value of 10^3 Ωm from the 3-D models rather than the value of 10^4 Ωm from the 2-D models. Moreover, in the 2-D models, the interface between the embankment and the resistive layer appears quite flat, while some interruptions appear in the 3-D results at several points (Fig. 18b) with clear uplifts towards the surface, especially at $X = 70$–90 m, that is confirmed by the uplift of the top of the ground level before SCPT17 in the geological scheme in Fig. 6(c). Information from the three SCPTs validate the 2-D and 3-D results because the maxima of the blow counts happen at the level of gravel and pebbles in correspondence of the top of the resistive layer. The blow counts are not always high inside the resistive layer because they may not be directly proportional to the resistivity at certain conditions, such as low stiffness, clay content variation and local lithology (S. Oh & C.-G. Sun 2008; K. Sudha *et al.* 2009; A. Devi *et al.* 2017; J.T.D. Gonçalves *et al.* 2021). This outcome may be used for further analysis on possible weak zones inside or below the embankment. The posterior analysis of the resistivity models is provided in Figs 16 and 17, panels (c) and (d). The sensitivity is high in the upper subsurface, that is, in the shallow conductive layer and in the underlying resistive layer (see also Fig. 18a), because near surface materials have large influence on the measured data. The sensitivity and resolution decrease with depth and, in fact, for both 2-D and 3-D results, the sensitivity is negative below 10 m of depth. In both 2-D and 3-D results, the resistive layer of the WS models had higher sensitivity than in the DD models. This can be explained by the acquisition sequences, that were customized to have the largest possible distance between the current electrodes of the WS quadrupoles. The sensitivity of the resistive region below the embankment is lower in 2-D than in 3-D, especially where the 2-D models present 10^4 Ωm (Figs 16c and d). This observation and geological information endorse that the 2-D results may have overestimated the resistivity in that region.

(ix) For both synthetic and field data, around 96 per cent of the total runtime of 3-D inversion was always taken in solving inverse equations. However, 3-D inversion of WS data required more than twice the runtime for that of DD data (see Tables 1, 4 and 6). A reason for this substantial difference can be found in the log file of the inversion execution ('R3t.out'): The number of measurements read is around 16k in DD data and around 27k in WS data, probably because ResIPy does not consider the reciprocal measurements in DD data.

(x) Regarding the computation of 3-D inversion, it should be said that the customized 3-D meshes prevented running the inverse modelling on a common laptop because the memory required by ResIPy was higher than 10 GB. As a result, 3-D inversion of ERT data that are several kilometres long may become computationally prohibitive. This should not be seen as a limitation, since nowadays 3-D geophysical inversion in complex/big domains is mostly performed in workstations or High Performance Computing (HPC) that are becoming easily accessible (W. Siripunvaraporn 2012; A. Martí *et al.* 2020; F. Pace *et al.* 2022). Another reason for fostering the adoption of 3-D inversion is that it yields more realistic values than 2-D inversion and that the 3-D detailed results are more adapt to high-resolution interpretations (A. Vergnano *et al.*). Moreover, 3-D forward modelling, that is not computationally demanding, is more accurate than 2-D forward modelling and hence largely suitable for simulations of synthetic examples and sensitivity analyses.

8 CONCLUSIONS

We presented the results of 2-D and 3-D inversions of ERT data acquired over river embankments to identify local anomalies and prevent damages during floods. Both synthetic and field data were studied to evaluate the opportunity of performing 3-D instead of 2-D inversion of an ERT line acquired over peculiar geometries, such as a river embankment that is composed of a crest and slopes and whose longitudinal profile possibly curves. Synthetic data were generated with different electrode sequences (i.e. dipole−dipole and Wenner−Schlumberger) from a 3-D model representing a realistic embankment geometry with embedded anomalies. Field data were acquired close to Turin (NW Italy) over an embankment that has often been damaged by floods. To reproduce the specific 3-D geometry of the embankment, the 3-D models and meshes were customized in Gmsh, while the ERT forward and inverse modelling were performed in ResIPy.

Synthetic and field data were inverted in 2-D and 3-D, then the results were compared. The main outcomes demonstrate that, given an ERT line, the subsurface is better characterized by 3-D realistic models and 3-D inversion, especially if the data are acquired over complex or non-straight geometries. Moreover, from the synthetic examples it was evident that, despite the long computation time, 3-D results are more sensitive than 2-D results to buried anomalies that are eccentric or far from the electrodes. From the field case study, it could be concluded that, given a curved ERT line, 3-D results are more realistic and in line with the known geology than 2-D results. These results suggest that the proposed approach of performing 3-D inversion instead of 2-D inversion for a proper embankment characterization, even in presence of a 2-D ERT line, may represent a trade-off strategy that balances 2-D fast acquisition and 3-D inversion, that provides more realistic resistivity distributions than 2-D inversion.

An implication of these findings is that, for a complete characterization of the embankment in the transversal direction, a full 3-D approach (ERT data acquired in 3-D) would be preferable. Besides the embankments, the suggested approach can be beneficial for the

Downloaded from academic.oup.com/gji/article/247/3/ggag402/8853762 by guest on 16 November 2026

ERT characterization of earth dams, hills, abandoned mining dumps, trenches or landfills. Parallel research is focusing on combined interpretation of ERT and seismic measurements for river embankment screening, as part of the project GEOCHARME. Future work will consider the 3-D acquisition of ERT data to ensure a full 3-D approach from the field to the modelling.

ACKNOWLEDGMENTS

The research activity of FP was carried out within the Ministerial Decree no. 1062/2021 and received funding from the Fondo Sociale Europeo REACT-EU—PON Ricerca e Innovazione 2014–2020. The research activity of AV, CC, LVS was carried out within the ≪GEOCHARME≫ project, funded by the European Union—Next Generation EU and granted under the PRIN 2022 programme (D.D. 104–02/02/2022 Ministero dell'Università e della Ricerca). For the case study of field data, the authors thanks AIPO (Interregional Agency for the Po River, Moncalieri section) for sharing independent geotechnical data. The authors thank the reviewers for their valuable and helpful comments that helped us improve the manuscript.

AUTHOR CONTRIBUTIONS

- Conceptualization: F.P., A.A., A.V., C.C.
- Data curation: F.P., A.V.
- Investigation: A.V., C.C.
- Methodology: all
- Software: F.P., A.V.
- Supervision: A.A., A.G., C.C., L.V.S.
- Validation: F.P., A.A., C.C., A.V.
- Visualization: F.P., C.C., A.V.
- Writing—original draft: F.P.
- Writing—review and editing: all

SUPPORTING INFORMATION

Supplementary data are available at *GJIRAS* online.

Please note: Oxford University Press is not responsible for the content or functionality of any supporting materials supplied by the authors. Any queries (other than missing material) should be directed to the corresponding author for the paper.

DATA AVAILABILITY

The synthetic data presented in this article are publicly available in Zenodo, at https://doi.org/10.5281/zenodo.17965478. They represent the Supplementary Material of this article and are composed of:

(i) the ERT sequences,
(ii) the Python notebook to create the 3-D models and meshes,
(iii) the synthetic data and the results from 2-D and 3-D inversion of synthetic data.

The field data are part of the project GEOCHARME and will be made public in a devoted repository in the near future. In the meantime, the field data will be shared on reasonable request to the first author.

REFERENCES

Antoine, R., Fauchard, C., Fargier, Y. & Durand, E., 2015. Detection of leakage areas in an Earth embankment from GPR measurements and permeability logging, *Int. J. Geophys.,* **2015,** 1–9.

Arato, A., Vagnon, F. & Comina, C., 2022. First application of a new seismo-electric streamer for combined resistivity and seismic measurements along linearly extended earth structures, *Near Surf. Geophys.,* **20**(2), 117–134.

Arosio, D., Hojat, A., Ivanov, V.I., Loke, M.H., Longoni, L., Papini, M., Tresoldi, G. & Zanzi, L., 2018. A Laboratory experience to assess the 3D effects on 2D ERT monitoring of river levees, *Presented at the 24th European Meeting of Environmental and Engineering Geophysics,* pp. 1–5, European Association of Geoscientists & Engineers, Porto, Portugal. Available from: https://www.earthdoc.org/content/papers/10.3997/2214-4609.201802628.

Ball, J., Chambers, J., Wilkinson, P. & Binley, A., 2023. Resistivity imaging of river embankments: 3D effects due to varying water levels in tidal rivers, *Near Surf. Geophys.,* **21**(1), 93–110.

Bentley, L.R. & Gharibi, M., 2004. Two- and three-dimensional electrical resistivity imaging at a heterogeneous remediation site, *Geophysics,* **69**(3), 674–680.

Bièvre, G., Oxarango, L., Günther, T., Goutaland, D. & Massardi, M., 2018. Improvement of 2D ERT measurements conducted along a small earth-filled dyke using 3D topographic data and 3D computation of geometric factors, *J. Appl. Geophys.,* **153,** 100–112.

Downloaded from academic.oup.com/gji/article/247/3/ggag402/8853762 by guest on 16 November 2026

Binley, A., 2015. Tools and techniques: electrical methods, *Treatise on Geophysics [online]* , pp. 233–259 , Elsevier. Available from10.1016/B978-0-444-53802-4.00192-5, https://linkinghub.elsevier.com/retrieve/pii/B9780444538024001925.
Binley, A., 2023. *R2 User Guide (Version 4.10)*. [online]. Available from: http://www.es.lancs.ac.uk/people/amb/Freeware/R2/R2.htm.
Binley, A., 2024. *R3t User Guide*. [online]. Available from: http://www.es.lancs.ac.uk/people/amb/Freeware/R3t/R3t_readme.pdf.
Binley, A. & Kemna, A., 2005. DC resistivity and induced polarization methods, *Hydrogeophysics [online],* pp. 129–156, eds, Rubin, Y. & Hubbard, S. S., Springer-Verlag, Berlin. Available from10.1007/1-4020-3102-5_5, http://link.springer.com/10.1007/1-4020-3102-5_5
Binley, A. & Slater., L., 2020. *Resistivity and Induced Polarization: Theory and Applications to the Near-Surface Earth,* Cambridge University Press: Cambridge.
Blanchy, G., Saneiyan, S., Boyd, J., McLachlan, P. & Binley, A., 2020. ResIPy, an intuitive open source software for complex geoelectrical inversion/modeling, *Comput. Geosci.,* **137,** 104 423.
Boyd, J., Blanchy, G., Saneiyan, S., Mclachlan, P. & Binley, A., 2019. 3D geoelectrical problems with ResiPy, an open source graphical user interface for geoelectrical data processing, *Fast times,* **24**(4), 85–92.
Busato, L., Boaga, J., Peruzzo, L., Himi, M., Cola, S., Bersan, S. & Cassiani, G., 2016. Combined geophysical surveys for the characterization of a reconstructed river embankment, *Eng. Geol.,* **211,** 74–84.
Chambers, J.E. *et al.*, 2012. Bedrock detection beneath river terrace deposits using three-dimensional electrical resistivity tomography, *Geomorphology,* **177–178,** 17–25.
Chen, C., Liu, J., Xia, J. & Li, Z., 2006. Integrated geophysical techniques in detecting hidden dangers in river embankments, *J. Environ. Eng. Geophys.,* **11**(2), 83–94.
Comina, C., Vagnon, F., Arato, A. & Antonietti, A., 2020. Effective Vs and Vp characterization from Surface Waves streamer data along river embankments, *J. Appl. Geophys.,* **183,** 104 221.
Comina, C., Vagnon, F., Arato, A., Fantini, F. & Naldi, M., 2020. A new electric streamer for the characterization of river embankments, *Eng. Geol.,* **276,** 105 770.
Comina, C., Vergnano, A., Arato, A., Duò, E., Naldi, M., Chieppa, D. & Socco, V., 2026. *Dataset of a 4 km combined seismic and electric streamer survey along the embankment of the Po river in Crescentino*. [online]. Available from: https://essd.copernicus.org/preprints/essd-2026-32/. [Accessed 15 Jun 2026].
Comina, C., Vergnano, A., Arato, A., Naldi, M., Bigini, T., Chieppa, D. & Socco, L.V., 2025. A 4 Km Combined seismic and electric streamer survey along an embankment of the Po River, In: [online], *Presented at the NSG 2025: 4th Conference on Geophysics for Infrastructure Planning, Monitoring and BIM, Naples, Italy,* pp. 1–5, European Association of Geoscientists & Engineers, Available from: https://www.earthdoc.org/content/papers/10.3997/2214-4609.202520061.
Dahlin, T., 1996. 2D resistivity surveying for environmental and engineering applications, *First Break [online],* **14**(7). Available from: https://www.earthdoc.org/content/journals/10.3997/1365-2397.1996014.
Dahlin, T. & Loke, M.H., 1997. Quasi-3D resistivity imaging—mapping of three dimensional structures using two dimensional DC resistivity techniques, In: [online], *Presented at the 3rd EEGS Meeting, Aarhus, Denmark,* European Association of Geoscientists & Engineers. Available from: https://www.earthdoc.org/content/papers/10.3997/2214-4609.201407298.
Devi, A., Israil, M., Anbalagan, R. & Gupta, P.K., 2017. Subsurface soil characterization using geoelectrical and geotechnical investigations at a bridge site in Uttarakhand Himalayan region, *J. Appl. Geophys.,* **144,** 78–85.
Di Prinzio, M., Bittelli, M., Castellarin, A. & Pisa, P.R., 2010. Application of GPR to the monitoring of river embankments, *J. Appl. Geophys.,* **71**(2–3), 53–61.
Doyoro, Y.G., Chang, P.-Y., Puntu, J.M., Lin, D.-J., Van Huu, T., Rahmalia, D.A. & Shie, M.-S., 2022. A review of open software resources in python for electrical resistivity modelling, *Geosci. Lett.,* **9**(1), 1–16.
Floods Directive 2007. *tive 2007/60/EC of the European Parliament and of the Council of 23 October 2007 on the Assessment and Management of Flood Risks,* Publications Office of the European Union: https://eur-lex.europa.eu/legal-content/EN/ALL/?uri=CELEX%3A32007L0060. [online]. Direc 2007.
Geuzaine, C. & Remacle, J.-F., 2009. Gmsh: a 3-D finite element mesh generator with built-in pre- and post-processing facilities, *Int. J. Numer. Methods Eng.,* **79**(11), 1309–1331.
Gharibi, M. & Bentley, L.R., 2005. Resolution of 3-D electrical resistivity images from inversions of 2-D orthogonal lines, *J. Environ. Eng. Geophys.,* **10**(4), 339–349.
Ghosh, D., Banerjee, A., Puppala, A.J. & Kumar, P., 2024. Exploring the influence of climate change on Earthen embankments with expansive soil, *Geosciences,* **14**(2), 37.
Gonçalves, J.T.D., Botelho, M.A.B., Machado, S.L. & Netto, L.G., 2021. Correlation between field electrical resistivity and geotechnical SPT blow counts at tropical soils in Brazil, *Environmental Challenges,* **5,** 100 220.
Günther, T., Rücker, C. & Spitzer, K., 2006. Three-dimensional modelling and inversion of DC resistivity data incorporating topography—II. Inversion, *Geophys. J. Int.,* **166**(2), 506–517.
Hansen, C.D. & Johnson, C.R., 2005. *ParaView: An End-User Tool for Large Data Visualization, The Visualisation Handbook,* Elsevier-Butterworth Heinemann, Amsterdam, Boston.
Hojat, A., 2024. An iterative 3D correction plus 2D inversion procedure to remove 3D effects from 2D ERT data along embankments, *Sensors,* **24**(12), 3759.
Hojat, A., Arosio, D., Ivanov, V.I., Loke, M.H., Longoni, L., Papini, M., Tresoldi, G. & Zanzi, L., 2020. Quantifying seasonal 3D effects for a permanent electrical resistivity tomography monitoring system along the embankment of an irrigation canal, *Near Surf. Geophys.,* **18**(4), 427–443.
Hung, Y.-C., Lin, C.-P., Lee, C.-T. & Weng, K.-W., 2019. 3D and boundary effects on 2D electrical resistivity tomography, *Appl. Sci.,* **9**(15), 2963.
Karl, L., Fechner, T., Schevenels, M., François, S. & Degrande, G., 2011. Geotechnical characterization of a river dyke by surface waves, *Near Surf. Geophys.,* **9**(6), 515–527.
Koefoed, O., 1979. *Geosounding Principles 1 : Resistivity sounding measurements,* Elsevier Science Publishing Company, Amsterdam.
Kovačević, M.S., Jurić Kaćunić, D., Librić, L. & Bačić, M., 2018. Risk assessment in reconstruction of flood protection embankments due to climate change, *ce/papers,* **2**(2–3), 329–334.
Loke, M.H., 2004. *Tutorial: 2-D and 3-D Electrical Imaging Surveys*. [online]. Available from: https://sites.ualberta.ca/~unsworth/UA-classes/223/loke_course_notes.pdf.

Downloaded from academic.oup.com/gji/article/247/3/ggag402/8853762 by guest on 16 November 2026

Loke, M.H., Chambers, J.E., Rucker, D.F., Kuras, O. & Wilkinson, P.B., 2013. Recent developments in the direct-current geoelectrical imaging method, *J. Appl. Geophys.,* **95,** 135–156.

Lysdahl, A.K., Bazin, S., Christensen, C., Ahrens, S., Günther, T. & Pfaffhuber, A.A., 2017. Comparison between 2D and 3D ERT inversion for engineering site investigations—a case study from Oslo Harbour, *Near Surf. Geophys.,* **15**(2), 201–209.

Martí, A., Queralt, P., Marcuello, A., Ledo, J., Rodríguez-Escudero, E., Martínez-Díaz, J.J., Campanyà, J. & Meqbel, N., 2020. Magnetotelluric characterization of the Alhama de Murcia Fault (Eastern Betics, Spain) and study of magnetotelluric interstation impedance inversion, *Earth Planets Space,* **72**(1), 16.

Martorana, R. & Capizzi, P., 2023. Evaluation of artifacts and misinterpretation in 2D electrical resistivity tomography caused by three-dimensional resistive structures of regular or irregular shapes, *Appl. Sci.,* **13**(3), 2015.

Martorana, R., Capizzi, P., D'Alessandro, A. & Luzio, D., 2017. Comparison of different sets of array configurations for multichannel 2D ERT acquisition, *J. Appl. Geophys.,* **137,** 34–48.

Negri, S., Leucci, G. & Mazzone, F., 2008. High resolution 3D ERT to help GPR data interpretation for researching archaeological items in a geologically complex subsurface, *J. Appl. Geophys.,* **65**(3–4), 111–120.

Nimmer, R.E., Osiensky, J.L., Binley, A.M. & Williams, B.C., 2008. Three-dimensional effects causing artifacts in two-dimensional, cross-borehole, electrical imaging, *J. Hydrol.,* **359**(1–2), 59–70.

Oh, S. & Sun, C.-G., 2008. Combined analysis of electrical resistivity and geotechnical SPT blow counts for the safety assessment of fill dam, *Environ. Geol.,* **54**(1), 31–42.

Pace, F., Martí, A., Queralt, P., Santilano, A., Manzella, A., Ledo, J. & Godio, A., 2022. Three-dimensional magnetotelluric characterization of the Travale Geothermal Field (Italy), *Remote Sens.,* **14**(3), 542.

Pace, F., Vergnano, A., Arato, A., Comina, C., Troiano, F., Godio, A. & Socco, L.V., 2025. Comparison of 2D vs 3D inversions of electric resistivity tomography data over river embankments, In: *NSG 2025: 31st Meeting of Environmental and Engineering Geophysics, Naples, Italy.* , pp. 1–5, [online], European Association of Geoscientists & Engineers. Available from: https://www.earthdoc.org/content/papers/10.3997/2214-4609.202520189.

Papadopoulos, N.G., Tsourlos, P., Tsokas, G.N. & Sarris, A., 2007. Efficient ERT measuring and inversion strategies for 3D imaging of buried antiquities, *Near Surf. Geophys.,* **5**(6), 349–361.

Perri, M.T., Boaga, J., Bersan, S., Cassiani, G., Cola, S., Deiana, R., Simonini, P. & Patti, S., 2014. River embankment characterization: the joint use of geophysical and geotechnical techniques, *J. Appl. Geophys.,* **110,** 5–22.

Rahimi, S., Wood, C.M., Coker, F., Moody, T., Bernhardt-Barry, M. & Mofarraj Kouchaki, B., 2018. The combined use of MASW and resistivity surveys for levee assessment: a case study of the Melvin Price Reach of the Wood River Levee, *Eng. Geol.,* **241,** 11–24.

Reynolds, J.M., 2011. *An Introduction to Applied and Environmental Geophysics,* 2nd ed., Wiley-Blackwell, Chichester, West Sussex; Malden, Massachusetts.

Rücker, C., Günther, T. & Spitzer, K., 2006. Three-dimensional modelling and inversion of DC resistivity data incorporating topography—I. Modelling, *Geophys. J. Int.,* **166**(2), 495–505.

Siripunvaraporn, W., 2012. Three-dimensional magnetotelluric inversion: an introductory guide for developers and users, *Surv. Geophys.,* **33**(1), 5–27.

Sudha, K., Israil, M., Mittal, S. & Rai, J., 2009. Soil characterization using electrical resistivity tomography and geotechnical investigations, *J. Appl. Geophys.,* **67**(1), 74–79.

Tikhonov, A. N. & Arsenin, V. Y., 1977. Winston, V. H., *Solutions of ill-posed problems,* John Wiley and Sons. Inc: New York.

Tresoldi, G., Arosio, D., Hojat, A., Longoni, L., Papini, M. & Zanzi, L., 2019. Long-term hydrogeophysical monitoring of the internal conditions of river levees, *Eng. Geol.,* **259,** 105 139.

Vagnon, F., Comina, C. & Arato, A., 2022. Evaluation of different methods for deriving geotechnical parameters from electric and seismic streamer data, *Eng. Geol.,* **303,** 106 670.

Vagnon, F., Comina, C., Arato, A., Chiappone, A., Cosentini, R.M. & Foti, S., 2022. Geotechnical screening of linear earth structures: electric and seismic streamer data for hydraulic conductivity assessment of the Arignano Earth Dam, Italy, *J. Geotech. Geoenviron. Eng.,* **148**(12), 04 022 105.

Vergnano, A., Comina, C., Yan, H., Chieppa, D., Deangeli, C. & Socco, L.V., 2025a. Clustering and petrophysics of combined resistivity and seismic measurements for river embankments screening, In: *NSG 2025: 4th Conference on Geophysics for Infrastructure Planning, Monitoring and BIM, Naples, Italy,* [online], pp. 1–5, European Association of Geoscientists & Engineers, Available from: https://www.earthdoc.org/content/papers/10.3997/2214-4609.202520052.

Vergnano, A., Franco, D., Merico, A., Pace, F., Uggè, S. & Comina, C., 2025b. Survey and sequence strategies for full-3D electrical resistivity tomography in archaeological sites: a case study on a Domus of the Roman Town of Augusta Bagiennorum (NW Italy), *Archaeological Prospection,* **33,** (1). 87–107.

White, A., Boyd, J., Wilkinson, P., Unwin, H.E., Wookey, J., Kendall, J.M., Binley, A. & Chambers, J., 2024. Assessing the effect of offline topography on electrical resistivity measurements: insights from flood embankments, *Geophys. J. Int.,* **239**(2), 1117–1132.

White, A., Wilkinson, P., Boyd, J., Wookey, J., Kendall, J.M., Binley, A., Grossey, T. & Chambers, J., 2023. Combined electrical resistivity tomography and ground penetrating radar to map Eurasian badger (Meles Meles) burrows in clay-rich flood embankments (levees), *Eng. Geol.,* **323,** 107 198.

Downloaded from academic.oup.com/gji/article/247/3/ggag402/8853762 by guest on 16 November 2026

© The Author(s) 2026. Published by Oxford University Press on behalf of The Royal Astronomical Society. This is an Open Access article distributed under the terms of the Creative Commons Attribution License (https://creativecommons.org/licenses/by/4.0/), which permits unrestricted reuse, distribution, and reproduction in any medium, provided the original work is properly cited.